Magic Angle Spinning NMR of Proteins: High-Frequency Dynamic Nuclear Polarization and ^{1}H Detection

Yongchao Su, Loren Andreas, and Robert G. Griffin

Department of Chemistry and Francis Bitter Magnet Laboratory, Massachusetts Institute of Technology, Cambridge, Massachusetts 02139; email: rgg@mit.edu

Annu. Rev. Biochem. 2015. 84:465–97

First published online as a Review in Advance on March 30, 2015

The *Annual Review of Biochemistry* is online at biochem.annualreviews.org

This article's doi: 10.1146/annurev-biochem-060614-034206

Keywords

NMR, dynamic nuclear polarization, protein structure, membrane proteins, amyloid fibrils, ^{1}H detection

Abstract

Magic angle spinning (MAS) NMR studies of amyloid and membrane proteins and large macromolecular complexes are an important new approach to structural biology. However, the applicability of these experiments, which are based on ^{13}C- and ^{15}N-detected spectra, would be enhanced if the sensitivity were improved. Here we discuss two advances that address this problem: high-frequency dynamic nuclear polarization (DNP) and ^{1}H-detected MAS techniques. DNP is a sensitivity enhancement technique that transfers the high polarization of exogenous unpaired electrons to nuclear spins via microwave irradiation of electron–nuclear transitions. DNP boosts NMR signal intensities by factors of 10^{2} to 10^{3}, thereby overcoming NMR's inherent low sensitivity. Alternatively, it permits structural investigations at the nanomolar scale. In addition, ^{1}H detection is feasible primarily because of the development of MAS rotors that spin at frequencies of 40 to 60 kHz or higher and the preparation of extensively ^{2}H-labeled proteins.

Contents

INTRODUCTION 466
MAGIC ANGLE SPINNING NMR OF BIOMACROMOLECULES 467
Magic Angle Spinning NMR of Membrane Proteins and Amyloid Fibrils 467
The Sensitivity Problem and Solutions 470
DYNAMIC NUCLEAR POLARIZATION 471
Evolution and Instrumentation 471
Mechanisms 473
Polarizing Agents and Protein Samples 477
DYNAMIC NUCLEAR POLARIZATION–ENHANCED NMR OF BIOMACROMOLECULES 478
Structure and Drug Binding of Membrane Proteins 478
Structure and Assembly Mechanism of Amyloid Fibrils 479
Whole Cells, Plant Cells, and Other Biomacromolecules 481
Line Width of Frozen Proteins 485
^{1}H-Detected Spectra at High Spinning Frequencies 485
CONCLUSIONS AND OUTLOOK 488

INTRODUCTION

Structural studies of membrane-associated proteins, pathological amyloid fibrils, and other large molecular complexes are frequently challenging because they lack long-range order, are insoluble, or both. In these cases, magic angle spinning (MAS) nuclear magnetic resonance (NMR) has evolved as a powerful and indispensable technique to provide atomic-resolution structural information (1–6). However, a major limitation of MAS NMR has concurrently appeared, that is, the inherently low sensitivity of the technique due to the fact that most of the experiments utilize detection of ^{13}C and ^{15}N. In order to address this problem, dynamic nuclear polarization (DNP) and ^{1}H detection have been proposed as approaches either separately or together (7–10). In particular, by transferring the high polarization of the electron spin reservoir to the nuclei of interest via microwave irradiation, DNP can boost the NMR intensity by factors of 10^2 to 10^3, leading to a time savings of 10^4 to 10^6. As a consequence, over the past 20 years, instrumentation for DNP (including subterahertz gyrotron microwave sources and MAS probes operating at the liquid-nitrogen temperature) has undergone intense development, leading to implementation of DNP experiments at magnetic fields of up to 18.8 T corresponding to a frequency of up to 800 MHz for ^{1}H. In addition, as discussed below, greater enhancements of polarization can be achieved by utilizing new biradical polarizing agents and partially deuterated protein samples (11).

^{1}H detection for MAS experiments has developed in parallel with DNP. In 1980, Bodenhausen & Ruben (12) introduced ^{1}H indirect detection schemes to solution NMR, and these techniques are now routine in liquid-state protein structure experiments. They yield an increase in sensitivity of $(\gamma_H/\gamma_X)^{3/2}N$, where γ are the gyromagnetic ratios of the ^{1}H and X nuclei (^{13}C, ^{15}N, etc.) being detected and N is the number of attached protons (13). Thus, for $-^{13}CH_3$, $-^{13}CH_2-$, and $-^{13}CH-$ groups, the sensitivity gains are 24, 16, and 8, respectively, and for $^{15}N^{1}H$ the gain is ~30. Although there have been many innovations and improvements on the original experiment, this increased sensitivity is essentially what enables determination of protein structures in solution, and it is now possible to perform similar MAS experiments. The instrumental developments that enable

their successful application are MAS rotors that spin at ≥40–60 kHz together with deuterated proteins in which ^{1}H is magnetically dilute—for example, present only as the back-exchanged amide ^{1}H. These two experimental advances have catalyzed the commercialization of MAS DNP NMR spectrometers and high-frequency spinning probes for ^{1}H detection. As discussed in this review, these sorts of increases in sensitivity are dramatically expanding the chemical and biological landscape that NMR can be used to explore.

This review provides an overview of DNP and ^{1}H detection and their use as signal-enhancement methods, with illustrations of the manner in which they contribute to the high-resolution structural elucidation of biologically and pathologically important systems. As an introductory background, we first discuss recent applications of advanced dipolar recoupling MAS NMR techniques in the high-resolution determination of protein structures and interactions. We then present the evolution of and most recent progress in DNP experiments, including the basic principles, instrumentation, polarizing agents, and preparation of protein samples. Specifically, we discuss the classic continuous-wave (CW)-DNP mechanisms, including the solid effect (SE) and the cross effect (CE), and we mention the recent observation of the Overhauser effect (OE). We also describe the recent technical improvements of the two most crucial instrumentation components, the microwave source and low-temperature probe. We then review the many applications of DNP-enhanced MAS NMR in studies of membrane proteins, amyloid fibrils, and other biological macromolecules in glassy matrices, and address how the structural parameters elucidate molecular mechanisms of biological function. Finally, we examine advances in the use of ^{1}H-detected MAS in the regime of high spinning frequencies, which is currently $\omega_r/2\pi \geq 40$–60 kHz.

MAGIC ANGLE SPINNING NMR OF BIOMACROMOLECULES

Magic Angle Spinning NMR of Membrane Proteins and Amyloid Fibrils

MAS NMR has been used for the structural elucidation of crystalline proteins (14–16) as well as for many other biological samples (17–19). Its indispensable role stems from its ability to both provide structural data on samples that lack long-range order and elucidate molecular dynamics on timescales ranging from picoseconds to seconds (3, 4, 20). It is therefore well suited to the study of biological samples that cannot be dissolved and easily crystallized, or for which crystallization is suspected to significantly alter the samples' function and biological significance. Examples of classes of molecules in this category include membrane proteins that function properly only when embedded in a bilayer membrane (21–25) and protein fibrils (19, 26–28) associated with neurodegenerative or other diseases.

Figure 1 depicts some of the architectural motifs of membrane proteins and amyloid fibrils. Membrane proteins represent one-third of the proteins encoded by the human genome and constitute more than 50% of the known protein targets for pharmaceutical interventions (29). These proteins conduct their biological functions in lipid membranes, which give rise to structural features that are distinct from those of globular proteins (**Figure 1*a–e***). For example, membrane proteins usually have a certain topology, defined as insertion depth and orientation. They interact with lipid through charge–charge or hydrophobic interactions (20, 30). Moreover, the impact of protein on the lipid membrane can be functionally relevant. This impact may include membrane disruption, membrane fusion, and pore formation. Nevertheless, the vast majority of membrane protein structures are unknown, due to the challenges of production and crystallization. Although progress has been made in the crystallization of membrane proteins, the conditions used for crystallization often differ significantly from native conditions, which can lead to substantial structural differences (31). Lipid membranes composed of hydrated phospholipid bilayers used

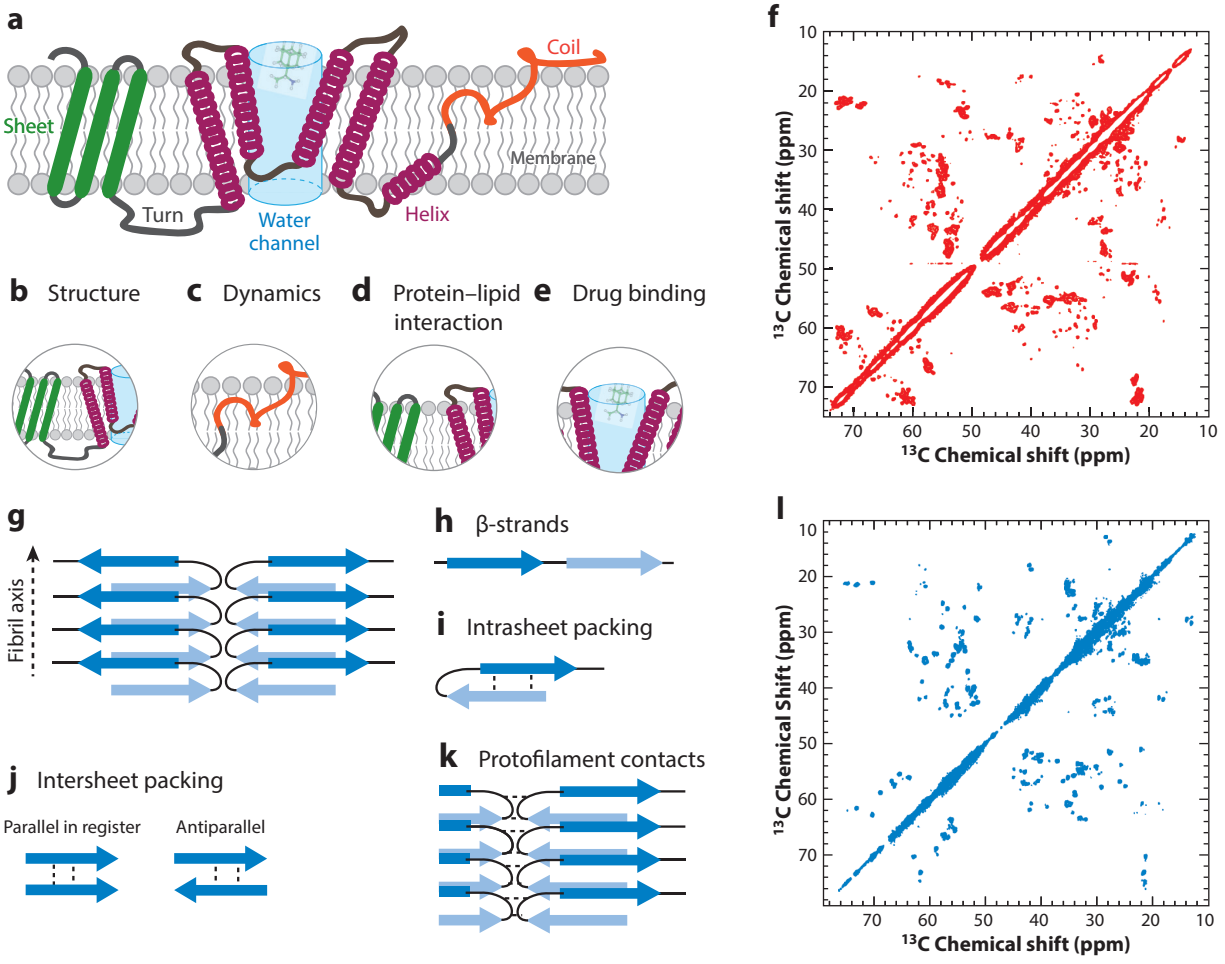

Figure 1

Structural topology of (*a–e*) membrane proteins and (*g–k*) amyloid fibrils, classes of samples that are particularly suited to study by MAS NMR. (*a*) A hypothetical membrane protein with α-helix, β-sheet, turn, and random coil domains. (*b–e*) Biofunctionally related structure, dynamics, and interactions in the characterization of membrane proteins that can be obtained by MAS NMR. (*g*) β-Structural assembly of amyloid fibrils. (*h–k*) Inter- and intramolecular contacts stabilizing the fibril assembly, including interactions between residues, strands, sheets, and protofilaments within the fibril architecture. Also shown are two representative ^{13}C–^{13}C RFDR spectra of (*f*) a membrane protein, VDAC (*red*), and (*l*) an amyloid protein, hβ_2m (*blue*), illustrating the excellent resolution that can be obtained for these classes of samples. Abbreviations: hβ_2m, human β_2 microglobulin; MAS, magic angle spinning; RFDR, radio-frequency-driven recoupling; VDAC, voltage-dependent anion channel.

in MAS and oriented-sample NMR structural studies most closely resemble the native cellular membrane. For example, membrane-bilayer-bound proteins such as bacteriorhodopsin (bR) (10, 32, 33), sensory rhodopsin (sR) (22, 34), voltage-gated potassium channels (Kv) (35, 36), voltage-dependent anion channels (VDAC) (37), G protein–coupled receptors (38), integral membrane proteins such as DsbA and DsbB (39), proton channels such as influenza M2 (2, 21, 40, 41), viral fusion proteins (2), and microbial retinal-binding photoreceptor (22) are biologically functional, enabling mechanistic studies of ion pumping, channel gating, and ligand binding with MAS

NMR. **Figure 1*f*** depicts a two-dimensional (2D) ^{13}C-^{13}C radio-frequency-driven recoupling (RFDR) spectrum of VDAC, a 283-amino-acid protein from the mitochondrial outer membrane.

Amyloid fibrils represent a second category of proteins that are well suited for MAS NMR experiments; they are usually β-strands that form β-sheets (or β-helices) that then assemble into Pauling cross-β structures. These structures are associated with more than 40 known human amyloid diseases (42, 43), including Alzheimer's disease, Parkinson's disease, type II diabetes, dialysis-related amylosis, Huntington's disease, and prion diseases. In addition to the pathological species, amyloid fibrils are also functional. An example is the major protein component of bacterial biofilms, CsgA (44). Amyloid fibrils exhibit three defining biophysical characteristics: (*a*) They bind Congo red and/or thioflavin T, (*b*) they exhibit long unbranched fibrils in electron micrographs measuring ~100 Å in diameter, and (*c*) they show a cross-β X-ray diffraction pattern with lines at ~4.7 Å and ~8–10 Å for strand–strand and sheet–sheet distances, respectively. Although all fibrils have a core β-sheet structure, they can possess other structural properties, such as loops and termini that exhibit various degrees of mobility. The fibril architecture can contain complicated structural features (**Figure 1*g–k***), which likely form the basis of the pathological assembly and, therefore, are critical for understanding the folding and self-assembly pathway. In addition, amyloid fibrils can be polymorphic (17, 45) and consist of mixtures of different proteins (46). Although amyloid fibrils are an important category of insoluble and noncrystalline proteins, their atomic-resolution structures are essentially inaccessible by solution NMR and X-ray diffraction; therefore, MAS NMR is the method of choice for characterizing these systems. Accordingly, several model and pathological fibrils have been characterized, including peptides derived from amyloid β (Aβ) (47–49) and transthyretin ($TTR_{105-115}$) (17), $A\beta_{1-40}$ (5), α-synuclein (50–52), Sup35p (53, 54), human prion protein (55), human β_2 microglobulin ($h\beta_2m$) (28, 56, 57), the SH3 domain of phosphoinositol 3-kinase (PI3-SH3) (58, 59) biofilms (60–62), and other peptides and proteins (59, 63, 64). The goal of these studies is to identify the fibril cores, registry of interstrand arrangements, and supermolecular organization. **Figure 1*l*** shows a typical spectrum from fibrils composed of $h\beta_2m$ and displays the excellent resolution of these microscopically ordered but macroscopically disordered samples.

As illustrated in the 2D spectra in **Figure 1**, MAS NMR has experienced tremendous advances in both instrumentation and experimental techniques. These advances have enabled the high-resolution structure determination of peptides [e.g., N-*formyl*-L-methionyl-L-leucyl-L-phenylalaninol (N-*f*-MLF-OH)] and proteins of relatively small size (e.g., SH3, CrH, G_{B1}), and continuing development has led to the characterization of larger and more significant proteins in native or near-native conditions (e.g., MMP12, sR). Sensitivity and resolution can be dramatically improved by performing experiments in high-field magnets (up to 23.5 T, 1,000 MHz for ^1H) with probes that spin at high MAS frequencies ($\omega_r/2\pi \sim 60$ kHz). In addition, new pulse sequences and detection techniques have emerged to record multidimensional homo- and heteronuclear correlation spectra. For example, one can establish through-space correlation by utilizing new dipolar recoupling methods such as proton-assisted recoupling (PAR), and proton-assisted insensitive nuclei cross-polarization (PAIN-CP) (65–69). These third-spin-assisted recoupling sequences (TSARs) (70), based on second-order recoupling and utilizing Hamiltonians that contain zero-quantum (ZQ) or double-quantum (DQ) heteronuclear operators, are not subject to dipolar truncation and thus provide efficient long-distance correlations. Several improved mixing schemes for homonuclear correlation have been published for the high-frequency MAS regime ($\omega_r/2\pi >$ 30 kHz), including mixed rotational and rotary resonance (MIRROR) (71), phase-alternated recoupling irradiation (PARIS) (72), and R2-symmetry-driven spin diffusion (RDSD) (73) and their variants.

In addition to dipolar-based techniques, strategies using through-bond correlation via *J* coupling have been successfully employed (74, 75). These scalar-based transfers are not attenuated by the molecular dynamics and thus provide complementary information to dipolar-based experiments. These techniques generally yield 4–6-Å distances that are useful for structural determination. Moreover, paramagnetic relaxation enhancement (PRE) methods have been introduced to MAS to measure distances up to 20 Å (76–79). Fast data acquisition can be achieved by use of nonuniform sampling (NUS) (80–82) and paramagnetic relaxation–assisted condensed data collection (PACC) (83). Selective and sparse isotopic labeling schemes have largely simplified the spectra and permit site-specific distance measurement (84–87). This substantial progress in developing hardware, experimental methods, and sample preparations for MAS NMR has resulted in many high-resolution structural characterizations of membrane proteins, amyloid fibrils, protein assemblies, and other proteins complexes. Finally, as discussed in more detail below, three-dimensional (3D) and four-dimensional (4D) $^{1}H/^{13}C/^{15}N$ experiments recorded at high fields and spinning frequencies using perdeuterated proteins with ^{1}H detection have displayed excellent resolution and signal-to-noise (S/N) ratios (88–90). In a recent example, the spectra of five different proteins were assigned using a suite of seven $^{1}H/^{13}C/^{15}N$-detection experiments (91).

The Sensitivity Problem and Solutions

As is clear from the above discussion, MAS NMR is an excellent nonperturbing approach to obtaining structural data on proteins and nucleic acids via ^{13}C–^{13}C, ^{13}C–^{15}N, ^{1}H–^{15}N, and ^{13}C–^{31}P dipolar recoupling. However, NMR signals are proportional to the Boltzmann polarization, $\sim\gamma\hbar B_0/2kT$, where γ, $\hbar$, B_0, k, and T denote the nuclear gyromagnetic ratio, Planck's constant divided by 2π, the magnetic field, Boltzmann's constant, and the temperature, respectively (95). The net population difference between spin energy levels amounts to ~0.01% for ^{1}H at ambient temperature. Thus, NMR signal intensities are small, and typical 3D experiments can require nearly a week of signal averaging. This problem is exacerbated by the fact that most proteins of interest have a high molecular weight, resulting in low sample concentrations in MAS NMR studies. In addition, modern multidimensional MAS NMR techniques usually lose signal during the evolution and mixing steps of a multidimensional experiment. Finally, due to the long nuclear spin lattice relaxation times, conventional experiments require seconds for thermal polarization recovery, leading to extended experimental acquisition times.

There are many ways to improve NMR sensitivity, embodied in the S/N ratio:

$$(S/N) \propto (n\gamma^{5/2} B_0^{3/2})/T,$$

where n is the total number of spins and the other symbols are as defined above. Thus, it is routine to increase n in the sample and to generate a larger population difference either by increasing the B_0 in which the NMR experiment is performed or by decreasing T to increase the Boltzmann factor. Subsequently, one can excite the spin system with a single pulse (**Figure 2*a***) to observe the NMR spectrum. This approach is used for nuclei with large magnetic moments, such as ^{1}H and ^{19}F, which have large γ and sufficient sensitivity to be utilized in direct observation. However, for relatively low-γ spins such as those of ^{13}C and ^{15}N, the signals are generally enhanced via transfer of polarization from ^{1}H via either *J*-based insensitive nuclei enhanced by polarization transfer (INEPT) (**Figure 2*b***) (92) or dipolar cross-polarization (CP) sequences (**Figure 2*c***) (93). In principle, both CP and INEPT can enhance the signal of the low-γ X spins by a factor of $\gamma_{^1H}/\gamma_X$, which is 4 or 10 for the case of ^{1}H to ^{13}C or ^{15}N transfer, respectively. It follows from these arguments that even larger signal enhancement can be achieved if the polarization is

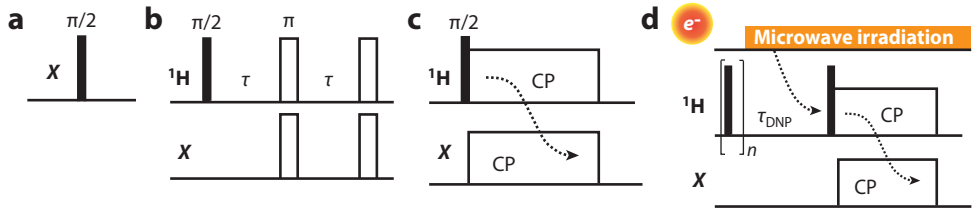

Figure 2

Pulse schemes of (*a*) DP and (*b–d*) signal-enhancement techniques via magnetization transfer. (*b*) INEPT (92), which establishes connectivity though J coupling. The magnetization transfer can be achieved if $\tau = (4 \cdot {}^1J_{HX})^{-1}$. (*b*) CP via ^{1}H–$X$ dipolar coupling (93). ^{1}H magnetization can be transferred to bonded or a nearby X spin via CP if the Hartmann–Hahn match condition is fulfilled ($\gamma_S \cdot B_{1S} = \gamma_{^1H} \cdot B_{1^1H}$, for spin-1/2 X spin). (*d*) DNP (94). Magnetization is transferred from an electron to ^{1}H via continuous microwave irradiation. Abbreviations: CP, cross-polarization; DNP, dynamic nuclear polarization; DP, direct polarization; INEPT, insensitive nuclei enhanced by polarization transfer; J, through-bond indirect coupling; B_{1S}, radio-frequency magnetic field applied to the S spin.

transferred from electrons to ^{1}H, given that $\gamma_{e-}/\gamma_{^1H} = 658$, or to other nuclei where this ratio is even larger. This is the basis of the DNP experiments that are the subject of this review. In particular, the large population difference of electron spins can be transferred to nuclear spins via microwave irradiation of the electron paramagnetic resonance (EPR) spectrum at the appropriate frequency (94). In practice, ^{1}H DNP enhancements on test samples have reached ~400 for the biradical AMUPol [15-{[(7-oxyl-3,11-dioxa-7-azadispiro[5.1.5.3]hexadec-15-yl)carbamoyl][2-(2,5,8,11-tetraoxatridecan-13-ylamino)]-[3,11-dioxa-7-azadispiro(5.1.5.3)hexadec-7-yl}oxidanyl, a PEGylated *bis*-TEMPO urea], 180 with TOTAPOL [1-(TEMPO-4-oxy)-3-(TEMPO-4-amino)propan-2-ol] at 380 MHz/250 GHz at 83 K, and 235 for the AMUPol biradical on a spectrometer (9, 96). These radicals are discussed further below, and their structures are shown in **Figure 6**. In samples of amyloid and membrane proteins, these values have ranged from ~10 to 75 (97, 98). However, as we learn to optimize sample preparation methods and improve the polarizing agents, we anticipate that the enhancements on relevant samples will continue to grow.

DYNAMIC NUCLEAR POLARIZATION

Evolution and Instrumentation

A modern DNP-MAS NMR spectrometer for biological studies involves the combination of a high-power microwave source, cryogenic cooling and MAS, polarizing radicals, and high-field magnets. In this section, we briefly discuss microwave components, cryogenics, and the MAS probe. The effect of polarizing agents and B_0 on the DNP enhancement is discussed in subsequent sections.

In 1953, only a few years after the discovery of NMR, Overhauser (99) proposed the concept of DNP, which was subsequently confirmed by Carver & Slichter's (100) experiments on lithium conducted in a 30.3-G magnetic field. This magnetic field corresponds to electron and nuclear Larmor frequencies of ~84 MHz and ~50 kHz, respectively, and were chosen because they are low frequencies and the spectrometer was simple to construct. Nevertheless, Carver & Slichter (100) observed an ~100-fold enhancement in the ^{7}Li signal, which provided the first experimental verification that electron polarization could be transferred to nuclear spins and enhance NMR signal intensities.

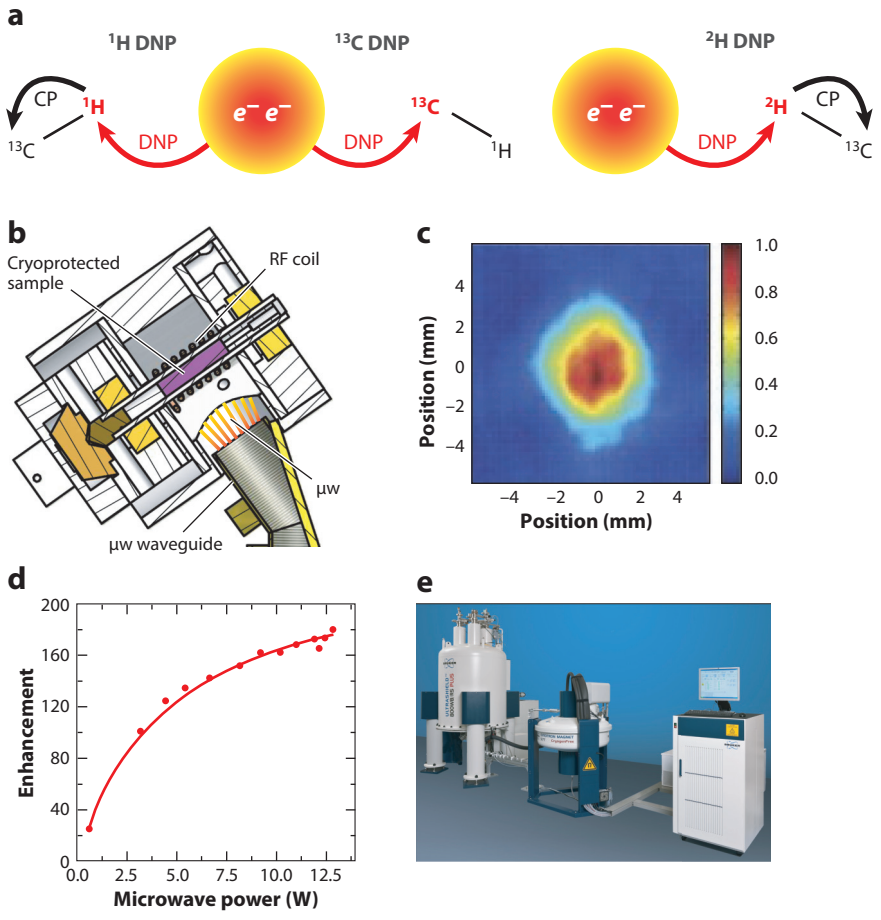

Figure 3

(*a*) Polarization transfer pathways from electrons to ^{1}H/^{13}C/^{2}H nuclei via DNP. (*b*) Diagram of the cryoprotected SSNMR sample within a MAS stator and under microwave irradiation for in situ DNP NMR experiments. (*c*) Linear intensity of an output millimeter beam recorded with a pyroelectric camera, showing the power distribution of the millimeter waves at a 250-GHz gyrotron (101). (*d*) Microwave power–dependent enhancement of the ^{13}C intensity of urea with 10 mM TOTAPOL at 80 K on a 380-MHz/250-GHz DNP NMR system (9). (*e*) A high-field DNP-enhanced SSNMR spectrometer operating at 800 MHz. Abbreviations: DNP, dynamic nuclear polarization; MAS, magic angle spinning; RF, radio-frequency; SSNMR, solid-state NMR; TOTAPOL, 1-(TEMPO-4-oxy)-3-(TEMPO-4-amino)propan-2-ol. Photograph in panel *e* provided by the Bruker Corporation.

During the next 30 years, the phenomenon of DNP was studied intensively with the primary scientific goal of producing polarized targets for nuclear scattering experiments (102, 103). During this era, many of the primary mechanisms for dynamically polarizing nuclei were discovered and exploited. For example, the SE (104–106), the CE (107–109), and thermal mixing (TM) (110) were thoroughly investigated in low-temperature experiments, and the OE was studied in systems with mobile electrons, such as conductors and solutions (111). In biological systems, one can transfer the large polarization in the electron spin reservoir directly to high-γ nuclei such as ^{1}H or to low-γ nuclei such as ^{13}C, ^{15}N, and ^{2}H (**Figure 3*a***). In addition, the electron polarization can be

indirectly transferred to ^{13}C, ^{15}N, and other biologically important nuclei by first polarizing ^{1}H and then performing a CP step, namely ^{1}H–*X* CP (**Figure 2*d***). Moreover, the polarization can be dispersed spatially over long distances (1,000–2,000 Å) in frozen biological solids via ^{1}H spin diffusion (112, 113).

In the late 1980s, Wind et al. (110), Yannoni and colleagues (114), and Schaefer and colleagues (115) integrated DNP into MAS NMR experiments using 40-GHz klystrons corresponding to ^{1}H frequencies of 60 MHz. Because of the low magnetic fields ($B_0 = 1.4$ T), these investigations were focused on polymers and other materials that yield relatively simple spectra. However, during this period biological NMR and MAS were transitioning rapidly to instruments using superconducting magnets ($B_0 > 5$ T), and performing DNP in these magnetic fields requires microwaves with frequencies ≥140 GHz ($\lambda \leq 2.14$ mm). This problem stimulated the development of gyrotrons—high-power, high-frequency microwave oscillators (116, 117)—for use in DNP because of their long lifetimes and operating frequencies that are scalable to ∼1 THz (118). Thus, these devices can be used for DNP experiments in high magnetic fields that are essential for studies of proteins and nucleic acids. Currently, the limit of 1 THz microwaves translates to 35.7 T or 1.52 GHz for the ^{1}H frequency.

Like X-ray crystallography, most DNP NMR experiments are conducted at cryogenic temperatures (80–100 K), optimizing the electronic and nuclear relaxation times (T_{1e}, T_{2e}, and T_{1n}) for efficient polarization transfer. The enhancement at 80 K is approximately four times higher than that at 110 K (9). Cryogenically cooled gases are used for the bearing and drive for MAS, and the current generation of the custom-designed heat exchanger directly cools dry N_2 gas to 80 K, with improved stable temperature control and low N_2 consumption (101, 119, 120).

The other crucial cryogenic apparatus is the NMR probe, which operates at liquid-nitrogen temperatures to allow MAS in the kilohertz regime, radio-frequency irradiation, microwave saturation, and sample insertion and ejection (120). The probe is enclosed in a vacuum-jacketed dewar that is required in order to achieve 80 K. **Figure 3*b*** depicts the MAS stator of the DNP-enhanced NMR instrumentation, and the microwaves are delivered perpendicular to the rotor axis. The corrugated waveguide and quasi-optics (121) transmit microwaves efficiently, have a low insertion loss, and have a high-quality microwave beam with >94% Gaussian content (**Figure 3*c***) (101). Increasing microwave power generally results in a larger DNP enhancement, as shown in **Figure 3*d*** for a 380-MHz/250-GHz DNP NMR system. Collectively, these advances in gyrotrons, microwave transmission lines, and cryogenic probe technology have enabled the operation of high-field DNP NMR spectrometers at 700 MHz/460 GHz (101) and a 800-MHz/527-GHz spectrometer that is commercially available (**Figure 4*e***).

Mechanisms

In CW-DNP experiments on solid dielectrics, the polarization transfer is mediated by four mechanisms: (*a*) the SE (106), (*b*) the CE (94, 107–109, 122–125), (*c*) TM (110), and (*d*) the recently observed OE (126, 127). Several papers (122, 128–132) and reviews (7, 125, 133) have provided in-depth descriptions of these mechanisms. In this section, we briefly review the two most important mechanisms applicable to proteins, the SE and CE. It is possible that future developments will lead to the emergence of the OE as an important DNP mechanism for proteins.

Whether the SE or CE serves as the dominant polarization mechanisms depends primarily on the EPR spectrum of the polarizing agent and its breadth compared with the nuclear Larmor frequency. These mechanisms can be understood quantum-mechanically with a system consisting of a small number of spins. Specifically, the SE is the dominant DNP mechanism when the breadth of the EPR spectrum is small compared with the nuclear Larmor frequency: $\delta, \Delta < \omega_n$, where δ

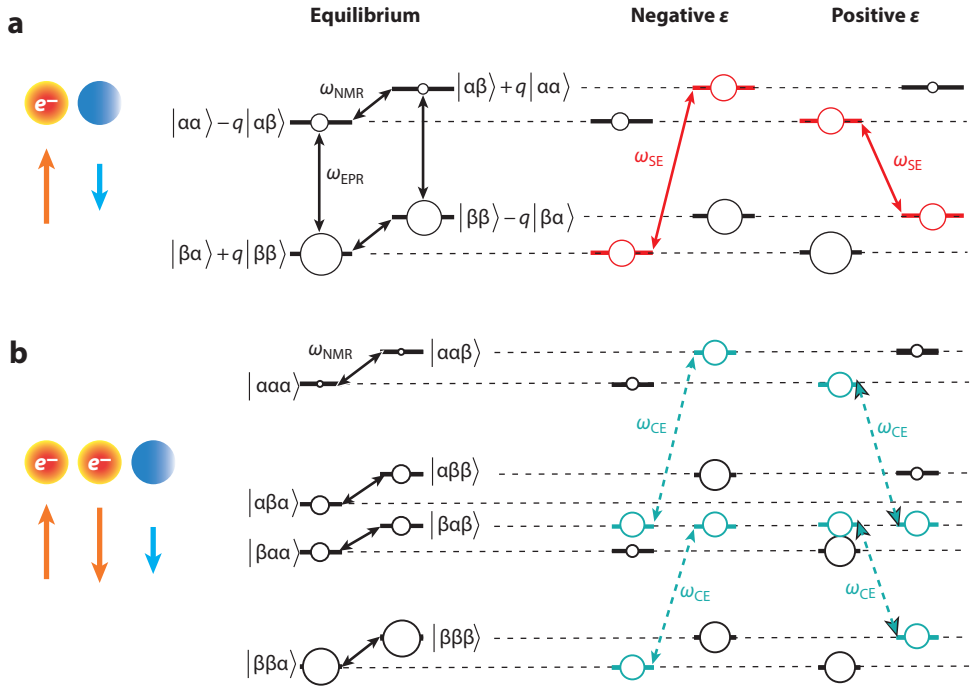

Figure 4

Energy-level diagrams illustrating conditions of equilibrium, positive enhancement, and negative enhancement in the presence of continuous microwaves that permit SE and CE mechanisms. (*a*) A coupled electron–nuclear spin pair that adopts the SE mechanism (104–106). The red arrows indicate the off-resonance microwave excitations that saturate the coupled states and lead to the DNP enhancement. ω_{NMR} and ω_{EPR} are the NMR and EPR frequencies, respectively. The mixing factor, q, comes from semisecular anisotropic hyperfine couplings. (*b*) A spin system of two electrons and a nuclear spin that allows DNP via the CE mechanism (94, 107–109, 122, 123). The enhanced nuclear polarization is deduced from the redistribution of the state-populations resulting from microwave excitations (*green arrows*) on resonance with EPR frequencies of two coupled electrons. Abbreviations: CE, cross effect; DNP, dynamic nuclear polarization; EPR, electron paramagnetic resonance; SE, solid effect.

and Δ are the homogeneous line width and inhomogeneous EPR line width, respectively, and ω_n is the nuclear Larmor frequency. When the microwave irradiation is applied at the frequency $\omega_\mu w = \omega_e \pm \omega_n$, where $\omega_\mu w$ and ω_e are, respectively, the microwave and EPR frequencies, then electron–nuclear spin flips are excited (**Figure 4*a***). The ZQ and DQ transitions yield negative and positive enhancements, respectively, as shown in **Figure 5*a***, which is the field profile for sulfonated 1,3-bisdiphenylene-2-phenylallyl (SA-BDPA), a radical that has a 28-MHz EPR line and, in this case, a ^{1}H Larmor frequency of 211 MHz. **Figure 6*a*** illustrates two other narrow-line radicals, trityl and BDPA, that yield SE enhancements. Note that the ZQ and DQ transitions are nominally forbidden and become allowed via mixing of nearby states by the terms in the dipolar Hamiltonian $H_{en} \sim q \cdot S_z I_\pm$. This process leads to a mixing coefficient of $|q| \sim (D_{en}/\omega_0)\omega_1$, and this term is squared to calculate the transition probability. Thus, the SE enhancement is proportional to ω_0^{-2} and decreases significantly at high fields. However, with large values of ω_1 it is possible to compensate for this loss.

In contrast, the CE is a three-spin process involving two dipolar coupled electrons, a nuclear spin, and an EPR spectrum whose breadth is larger than the ω_n. Thus, the CE becomes the

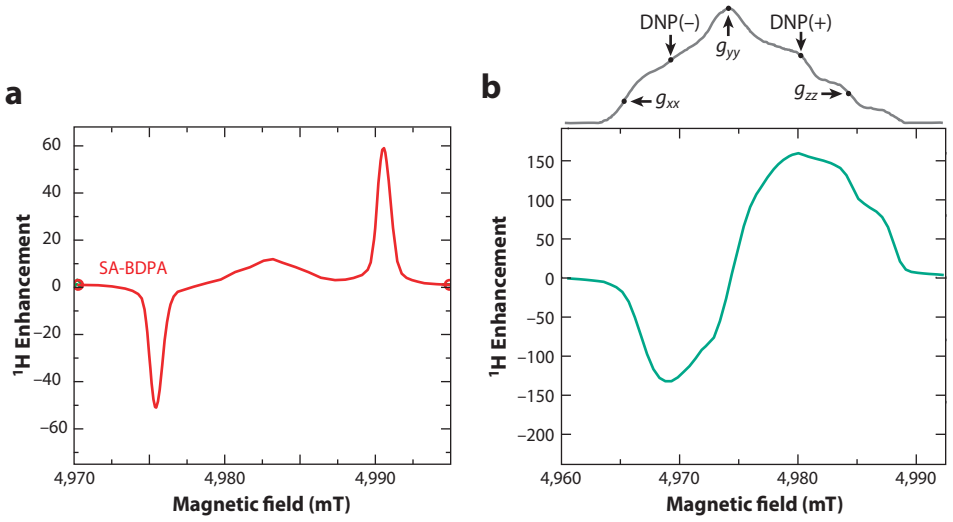

Figure 5

The field profiles of (*a*) SA-BDPA (126) and (*b*) bTbk (136) in glycerol/water, as a function of magnetic field, obtained on a custom-designed 211-MHz/140-GHz spectrometer. Each field profile shows positive and negative enhancements, but in panel *a* the SE governs the DNP process, whereas in panel *b* the CE dominates. SA-BDPA also shows an OE enhancement in the middle of the field profile. Abbreviations: bTbk, *bis*-TEMPO–*bis*-Ketal; CE, cross effect; DNP, dynamic nuclear polarization; SA-BDPA, sulfonated 1,3-bisdiphenylene-2-phenylallyl; SE, solid effect.

dominant mechanism when $\delta < \omega_n < \Delta$. The optimal transfer via this two-electron process occurs when $|\omega_{e1} - \omega_{e2}| = \omega_n$, where ω_{e1}, ω_{e2}, and ω_n are, respectively, the EPR resonance frequencies of the two electrons and the nuclear Larmor frequency (**Figure 4*b***) (94, 123, 128). At this "matching" EPR frequency separation, the $e^- e^-$ flip-flops are driven by the microwave irradiation and the difference in energy, ω_n, goes into the nuclear spin system. The matching condition leads to the requirement that the center two states $|\alpha\beta\alpha\rangle$ and $|\beta\alpha\beta\rangle$ be degenerate, permitting efficient DNP transfer at high fields. The matching condition is satisfied when spin isochromats in the sample satisfy this condition and when the number of spins doing so decreases as the operating frequency is increased. Thus, the CE scales as ω_0^{-1}. Finally, note that the above arguments for the CE assume a static sample, and the effect of sample rotation during MAS is to modulate the resonance frequency, as described by Maricq & Waugh (134, 135). In the case of a dipolar coupled biradical, the sample spinning results in different spin pairs satisfying the matching condition as the sample turns (130). The field profile for the *bis*-nitroxide biradical *bis*-TEMPO–*bis*-Ketal (bTbK) shown in **Figure 6*b*** is depicted in **Figure 5*b*** and illustrates the enhancement as a function of magnetic field.

To complete the discussion of CW-DNP mechanisms, we briefly describe TM and the OE. First, TM, which involves multiple electrons and a homogeneously broadened EPR line shape, becomes the dominant mechanism when $\Delta,\delta > \omega_{0I}$. Although TM was utilized extensively in early low-field DNP experiments, it has not yet become important in contemporary high-field experiments because the EPR spectra are inhomogeneously broadened. Second, the OE governs conducting systems or those involving mobile electrons, such as liquids, but it has been observed to become very inefficient at high fields (111). Most recently, two reports were published (126, 127) in which an OE effect was observed using the narrow-line radicals SA-BDPA in glycerol/

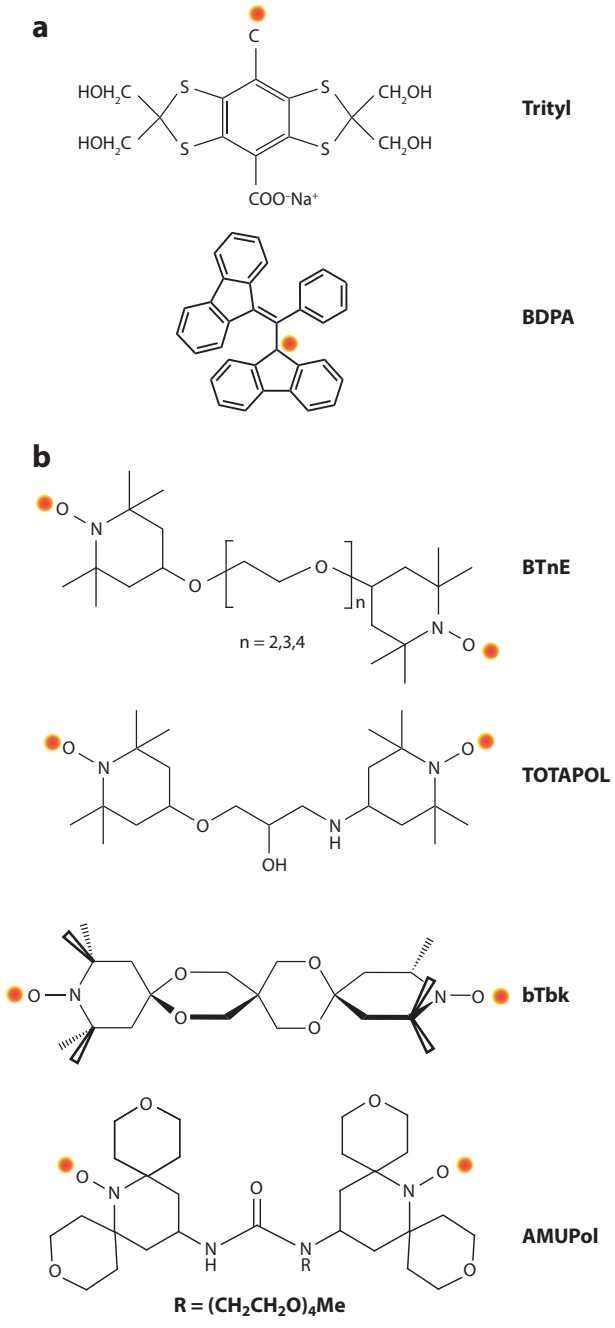

Figure 6

(*a*) Mono- and (*b*) biradicals and metal ions serving as polarization agents. Orange dots denote the unpaired electrons. To date, the biradicals TOTAPOL and, more recently, AMUPol have yielded the optimal enhancements via the cross effect mechanism. Abbreviations: AMUPol, 15-{[(7-oxyl-3,11-dioxa-7-azadispiro[5.1.5.3]hexadec-15-yl)carbamoyl]2-(2,5,8,11-tetraoxatridecan-13-ylamino)]-[3,11-dioxa-7-azadispiro(5.1.5.3)hexadec-7-yl}oxidanyl; BDPA, 1,3-bisdiphenylene-2-phenylallyl; bTbK, *bis*-TEMPO–*bis*-Ketal; bTnE, *bis*-TEMPO-*n*-ethyleneglycol; TOTAPOL, 1-(TEMPO-4-oxy)-3-(TEMPO-4-amino)propan-2-ol.

water and BDPA in polystyrene glassy matrices at high fields. In particular, the field profile in **Figure 5*a*** shows an OE effect manifested as a positive enhancement at the center frequency, and Can et al. (127) found that this enhancement increases linearly with ω_0 but requires the presence of ^{1}H hyperfine couplings in the EPR spectra. With the development of additional radicals with large hyperfine couplings that are stable in aqueous solution, the OE may become the method of choice for DNP experiments on proteins.

Polarizing Agents and Protein Samples

As mentioned above, the DNP-enhancement mechanisms require unpaired electrons that are generally not present in NMR samples. Thus, mono- and biradicals, which provide unpaired electrons, are usually exogenously doped into the samples of interest; the molecular structures of some of the radicals used for DNP are shown in **Figure 6*a*,*b***. These polarizing agents are preferably water soluble and uniformly dispersed in frozen solutions when glycerol is added for the purpose of forming a glass and cryoprotecting the protein. The preferred solvent composition—60% d_8-glycerol/30% D_2O/10% H_2O, known affectionately in the parlance of the trade as DNP juice—has been determined empirically to optimize the DNP enhancements. As discussed above, the DNP-enhancement mechanism depends on the choice of polarizing agents (11). Narrow-line monoradicals such as trityl and BDPA, which have nearly isotropic g-tensors, exhibit primarily an SE mechanism (**Figure 5*a***). At $\omega_n/2\pi = 211$ MHz/140 GHz DNP NMR, trityl and BDPA have EPR spectral breadths of ~90 and 28 MHz, respectively. In contrast, nitroxide (TEMPO) biradicals, including *bis*-TEMPO-*n*-ethyleneglycol (BTnE) (122), TOTAPOL (137), bTbk (136), and AMUPol (96), exhibit axially symmetric line shapes due to the g-anisotropy with $\Delta \sim 600$ MHz. Tuning the molecular tethers within the biradicals optimizes the performance of these molecules as polarizing agents. In particular, the tether determines the relative orientation of TEMPO rings and the degree to which the matching condition is fulfilled. For example, in the case of bTbk the nitroxide rings are locked in a fixed orientation with respect to one another, whereas TOTAPOL allows the possibility of rotation around the bonds of the tether. Furthermore, the interelectron distance determined by the length of the tether determines the e^-e^- dipole coupling. This coupling is ~22 MHz in TOTAPOL and ~35 MHz in AMUPol, which is based on a urea linker. The tetrahydropyran rings in AMUPol are substituted for the 4-methyl groups in TEMPO; they lengthen the T_{1e} and T_{2e} and increase the enhancement. To date, AMUPol has delivered a record enhancement of 420 in a urea sample at 250 GHz/380 MHz (Q. Ni & R.G. Griffin, unpublished results).

It is also important to recall that unpaired electrons interact with neighboring nuclear spins via the magnetic dipole–dipole interaction (138). These interactions lead to enhanced relaxation, sometimes referred to as PRE (139). The enhanced spin–spin relaxation due to PRE can be a nonnegligible contribution to line broadening in DNP NMR experiments and can cause significant signal quenching (140). To achieve a reasonable DNP enhancement and minimize the paramagnetic broadening, one should use a diluted concentration of radicals. The use of biradical polarizing agents such as TOTAPOL results in a much lower electron concentration compared with monoradicals such as TEMPO. For example, a concentration of 10 to 20 mM electrons (5 to 10 mM TOTAPOL or AMUPol) has been used in many DNP NMR studies. In addition, deuteration of solvent and protein samples has provided another way to improve DNP performance. The smaller ^{1}H reservoir can be polarized relatively more completely, resulting in better DNP performance. This enhanced DNP transfer has been employed for different proteins including the α-spectrin–SH3 domain (141) and bR (142, 143).

Table 1 Representative peptides, proteins, cells, and membrane complexes in DNP NMR studies

Biosystem	ε	Temperature (K)	Radical (mM)	B_0 (^{1}H frequency)	Reference
GNNQQNY	20	100	TOTAPOL (35)	400 MHz	56
TTR105–115	12	100	TOTAPOL (10)	400 MHz	144
PI3-SH3	30	100	TOTAPOL (10)	400 MHz	58
Aβ1–40	20	96	TOTAPOL (30)	400 MHz	145
Peptidoglycan	8.8	100	TOTAPOL (~80)	400 MHz	146
hΦ17W	18	100	bTbK[a]	400 MHz	147
M218–60	2.5	100	TOTAPOL (4)	600 MHz	97
Arabidopsis cell wall	27	100	TOTAPOL (35)	600 MHz	148
Mistic	20–30	100	TOTAPOL (30–40)	400 MHz	149
Whole cells	10	100	TOTAPOL (60)	400 MHz	150
Cell envelopes	26	100	TOTAPOL (60)	400 MHz	150
Ribosome	25	100	TOTAPOL (20)	400 MHz	151
Cell wall	20–40	100	TOTAPOL (1)	400 MHz	146
Escherichia coli SecYEG	32	100	TOTAPOL (20)	393 MHz	152
nAChR-bound NTII	26	100	TOTAPOL (50)	400 MHz	153
Apoferritin	20	90	TOTAPOL (1)	212 MHz	154
T2SS needles	30	104	TOTAPOL (28)	600 MHz	155
bR	75	83	AMUPol (40)	380 MHz	32

[a]40 μg *bis*-TEMPO–*bis*-Ketal (bTbK) in 6 mg 1-palmitoyl-2-oleoylphosphatidylcholine (POPC) containing 5 mol% peptide. Abbreviations: AMUPol, 15-{[(7-oxyl-3,11-dioxa-7-azadispiro[5.1.5.3]hexadec-15-yl)carbamoyl][2-(2,5,8,11-tetraoxatridecan-13-ylamino)]-[3,11-dioxa-7-azadispiro(5.1.5.3)hexadec-7-yl}oxidanyl; Aβ, amyloid β; B_0, magnetic field; bR, bacteriorhodopsin; DNP; dynamic nuclear polarization; nAChR, nicotinic acetylcholine receptor; NTII, neurotoxin II; PI3-SH3, the SH3 domain of phosphoinositol 3-kinase; TOTAPOL, 1-(TEMPO-4-oxy)-3-(TEMPO-4-amino)propan-2-ol; TTR, transthyretin; T2SS, type II secretion system; ε, DNP enhancement.

DYNAMIC NUCLEAR POLARIZATION–ENHANCED NMR OF BIOMACROMOLECULES

Although MAS NMR is a prime technique for structural characterization of insoluble and non-crystalline proteins, sensitivity is often the limiting factor in the study of higher–molecular weight complexes. Thus, the field of biological solid-state NMR is currently focused on complexes with asymmetric units of several tens of kilodaltons. In the past decade, several different systems have been investigated with DNP-enhanced MAS NMR, including crystalline proteins, membrane proteins, amyloid fibrils, and other species. **Table 1** summarizes some representative examples, showing that the intensity is enhanced by a factor of 10 to 40 at TOTAPOL concentrations of 10 to 35 mM recorded with 400- or 600-MHz spectrometers. In the following subsections, we review these studies to illustrate the role of DNP in the characterization of structures and interactions. Note that none of the proteins were ^{2}H labeled and all of the experiments used TOTAPOL, which was the first successful water-soluble biradical polarizing agent. In the case of α-spectrin–SH3 and bR, the enhancements were larger by a factor of two to four with the use of ^{2}H labeling and the use of AMUPol, rather than TOTAPOL.

Structure and Drug Binding of Membrane Proteins

A primary application of DNP has involved membrane proteins (33, 58, 97, 120, 142, 143, 156, 157), in which the structural details of active sites and ligand-binding sites have been efficiently

investigated. At ambient temperatures, many biological samples undergo dynamic processes that modulate the dipole coupling and can reduce the measured coupling or attenuate the coupling entirely. The low (≤100-K) temperatures used in DNP experiments can quench such dynamic processes, allowing the precise measurement of internuclear distances. The technique has been successfully applied to bR and influenza A $M2_{18-60}$, enabling precise measurements of structurally important distances (97, 120). Several additional applications have involved the determination of sequence-specific protein assignment (149, 152) and preparation of oriented samples (147), both of which are often the rate-limiting steps in the determination of 3D structures.

bR is a 26-kDa light-driven ion pump that can be trapped at several photocycle intermediates, providing the opportunity to determine the mechanism of ion conduction. In *Halobacterium salinarum*, bR is abundant in the cellular membrane, where it uses light energy to establish a proton gradient, thereby providing chemical energy to the cell. At the core of the protein, the active-site retinal absorbs light, causing a series of conformational changes that produce ion translocation, the detailed mechanism of which is not understood. Mak-Jurkauskas et al. (10) and Bajaj et al. (32) utilized DNP to study the retinal-binding site of bR and observed a series of trapped intermediates in the photocycle: bR_{555}, bR_{568}, L, and M_{412}. In the important L intermediate, which is present immediately prior to discharge of the H^+ from the Schiff base, four substates were resolved with DNP-enhanced spectra. The authors showed that one of these states is the functional L state, whereas the others are shunt states that convert to bR_{568} above a temperature of 170 K (**Figure 7*a*,*b***). Identifying the resonances in each state is the first step in determining the geometries of each state and understanding the conduction mechanism. These states occur in <20% of the protein, so they are virtually impossible to detect without low-temperature trapping and DNP.

The ultimate goal of these studies is to determine structurally important distances and torsion angles in order to understand the mechanism of ion translocation. Barnes et al. (120) showed that with the sensitivity afforded by DNP, precise distances can be measured in the active site of bR, which at 26 kDa is large by solid-state NMR standards. At thermal equilibrium, bR is found in two states, bR_{555} and bR_{568}, dividing the potential signal. Despite these challenges, DNP-enhanced RFDR spectra recorded as a function of mixing time were used to precisely measure the C15 = Nζ distance in both of these states. The resulting distances are 3.90 ± 0.08 Å for bR_{568} and 3.11 ± 0.22 Å for bR_{555}. These results demonstrate the power of DNP in the measurement of structurally important distances, and similar measurements applied to other states of bR will shed light on the conduction mechanism.

The M2 channel from influenza A assembles as a dimer of dimers, and conduction of protons at low pH is a key step in the infection pathway. Aminoadamantyl inhibitors reduce proton conduction by binding to the pore of the channel, which inhibits the invading virus. Through the use of DNP, a precise distance between the functional amine group of the drug and a protein Cα resonance was determined for the first time using a Z-filtered transfer echo double resonance (ZF-TEDOR) approach (**Figure 7*c*–*e***) (97). Similar to the case of bR, the low temperature in the DNP experiment was important for quenching the dynamic processes that prevented the observation of cross-peaks between the drug and the protein at high temperature. In this case, these additional cross-peaks likely arose from nonpharmacological interactions; however, they demonstrated the utility of DNP for probing weak interactions.

Structure and Assembly Mechanism of Amyloid Fibrils

Several amyloid fibrils that have been studied with DNP NMR include GNNQQNY from yeast prion Sup35 (112), $TTR_{105-115}$ (17, 144), PI3-SH3 (58) and $A\beta_{1-40}$ (145) (**Table 1**)

(**Figure 8**). As shown by the microwave-on and -off spectral comparison in **Figure 8*a***, ε = 35 and ε = 20 were obtained for the fibril forms of a seven-residue peptide GNNQQNY and the 99-residue protein hβ_2m, respectively (112). In the case of GNNQQNY, the value ε = 35 suggests that the 2D spectrum can be acquired 1,225 (35^2) times faster than under high-temperature conditions. **Figure 8*c*** shows that TTR peak assignments can be readily obtained

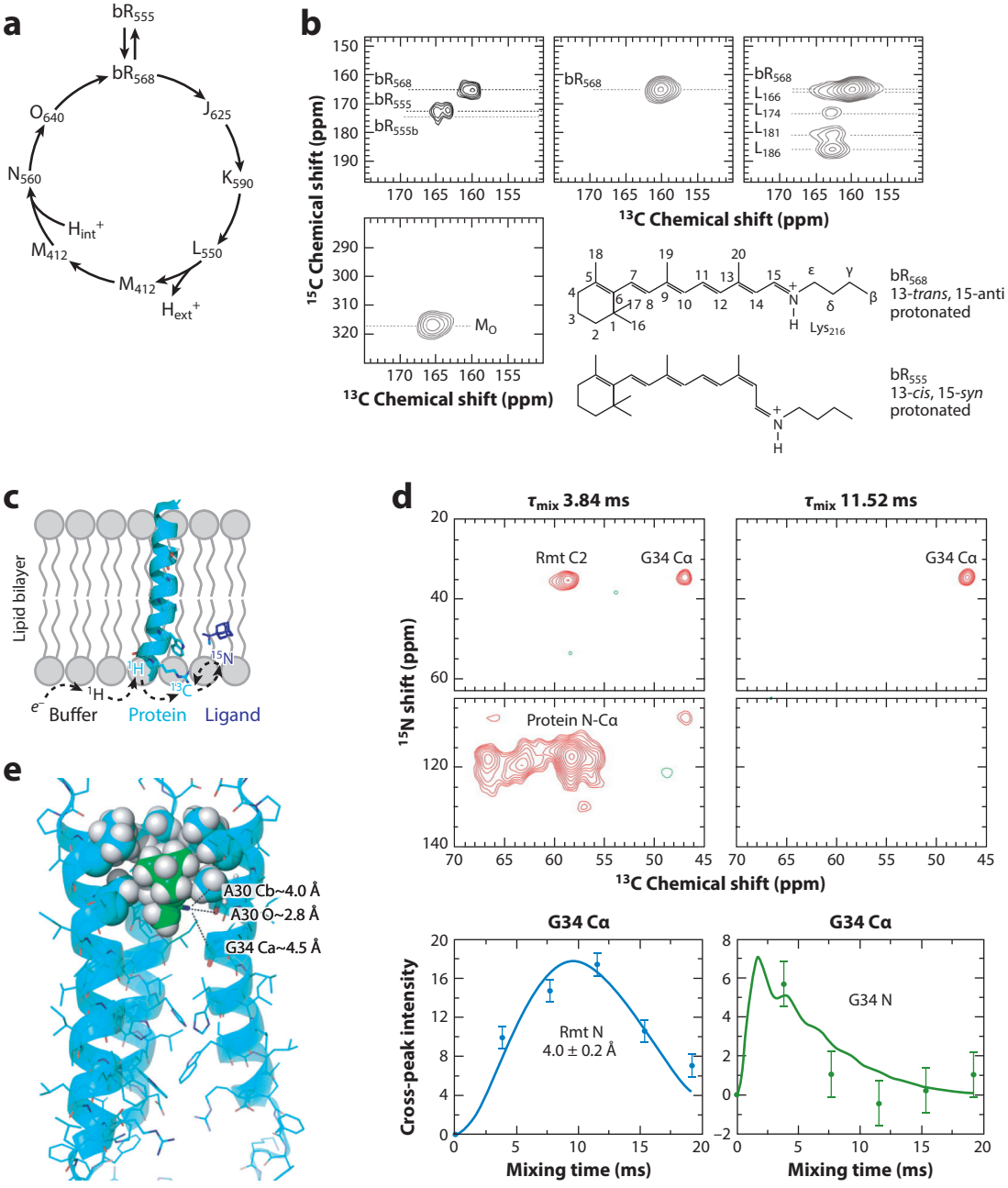

from the low-temperature spectrum acquired using DNP NMR and distances measured to high precision.

In addition to facilitating resonance assignments, the use of DNP in fibril studies can also expedite the correlation and measurement of long distances that are important for constraining inter- or intramolecular packing. For example, interstrand and intersheet contacts that describe the intermolecular packing between monomeric proteins are essential structural features in fibrils. It appears that most proteins adopt a parallel-in-register (PIR) arrangement, whereas small amyloidiogenic peptides can exhibit both parallel and antiparallel packing (158). These interstrand distance measurements led to the first complete structure of an amyloid fibril based on 10 MAS NMR constraints per residue shown in **Figure 8*d*** (17, 144). In proteins, the register of the strands can also be provided by MAS NMR using mixed fibril samples composed of [^{13}C,^{14}N]-labeled proteins prepared from 2-^{13}C-glycerol and [^{12}C,^{15}N] monomers prepared from $^{15}NH_4Cl$ in a one-to-one molar ratio (26, 56, 59). In such a sample, the Cα sites are heavily labeled by the 2-^{13}C-glycerol; therefore, the ^{15}N–^{13}Cα cross-peaks must arise from intermolecular contacts. If the assignments of Cα and amide ^{15}N are known, then these cross-peaks can establish the alignment of the proteins in the fibril. However, the intersheet distance between backbone spin pairs is ~5 Å and requires observation of small heteronuclear dipolar couplings of ~20 to 50 Hz. Observation of the resulting low cross-peak intensity significantly extends the acquisition time, and even then the spectra are not of high quality. We have successfully determined the intermolecular packing of PI3-SH3 fibrils by combining DNP with this approach (**Figure 8*c–e***) (58). The increased sensitivity from DNP [$\varepsilon = 30$ (**Figure 8*c***)] shortened the data-acquisition time of the long-mixing ZF-TEDOR experiment from days to hours and yielded numerous ^{15}N–^{13}C intrasheet constraints (**Figure 8*d***). The 52 interstrand contacts established from the DNP-enhanced spectra have successfully determined the PIR packing of PI3-SH3 fibrils and have constrained a preliminary structural model (**Figure 8*e***). In addition to the intensity enhancement of DNP, this experiment benefits significantly from the low temperature, which quenches the molecular motion. The spectrum shows a dramatic temperature dependence particularly in the aromatic region, where the cross-peaks are completely absent at high temperature and are well populated at 100 K. Similarly many extra cross-peaks appear in the NCO (amide-carbonyl) and NCA (amide-C_α) regions of the spectrum. The alignment of strands in fibrils can also be established with 1-^{13}C-glucose (159) and specific ^{13}C labeling (160, 161).

Whole Cells, Plant Cells, and Other Biomacromolecules

It has long been understood that membrane proteins function optimally when embedded in an Lα-phase membrane (23–25). Ideally, cellular machinery would be studied in such a biological context, but limited sensitivity typically dictates that the molecule of interest be more concentrated

Figure 7

Representative DNP-enhanced SSNMR studies of membrane proteins. (*a*,*b*) Spectroscopic evidence of contacts between the Schiff base and the retinal chromophore of bR (32). (*c–e*) Drug–protein interactions in membrane-bound M2 via distance measurements (97). (*a*) The mechanistic depiction of the ion-motive photocycle of bR. The subscripts denote the wavelength (in nanometers) of maximum visible absorption. (*b*) Assignments of retinal C15 in the different states of dark-adapted bR via 2D ^{15}Nζ–^{13}C correlation experiments. The structure of the retinal chromophore is shown for two of the states. (*c*) Cryoprotected M2 proteins in 5 mM TOTAPOL. (*d*) Representative ^{15}N–^{13}C ZF-TEDOR spectra and buildup curve to extract intermolecular distances that determine the binding site of the inhibitor rimantadine. (*e*) The rimantadine–M2 channel-binding model from distances that were obtained in DNP-enhanced experiments. Abbreviations: bR, bacteriorhodopsin; DNP, dynamic nuclear polarization; SSNMR, solid-state NMR; ZF-TEDOR, Z-filtered transfer echo double resonance; TOTAPOL, 1-(TEMPO-4-oxy)-3-(TEMPO-4-amino)propan-2-ol; 2D, two-dimensional.

and labeled. As such, typical biological NMR investigations purify the molecule of interest and, in the case of membrane proteins, use membrane mimetics that are often composed of detergents or phospholipids. In addition to protein studies, the complete structural characterization of cellular membrane includes detailed knowledge of the interaction among lipids, sugars, and embedded integral and peripheral proteins and is critical for understanding the associated molecular mechanisms such as signaling and recognition. With the increased sensitivity of DNP, two recent applications have demonstrated the utility of the approach in detecting protein signals and determining intermolecular associations within whole cells (146, 150).

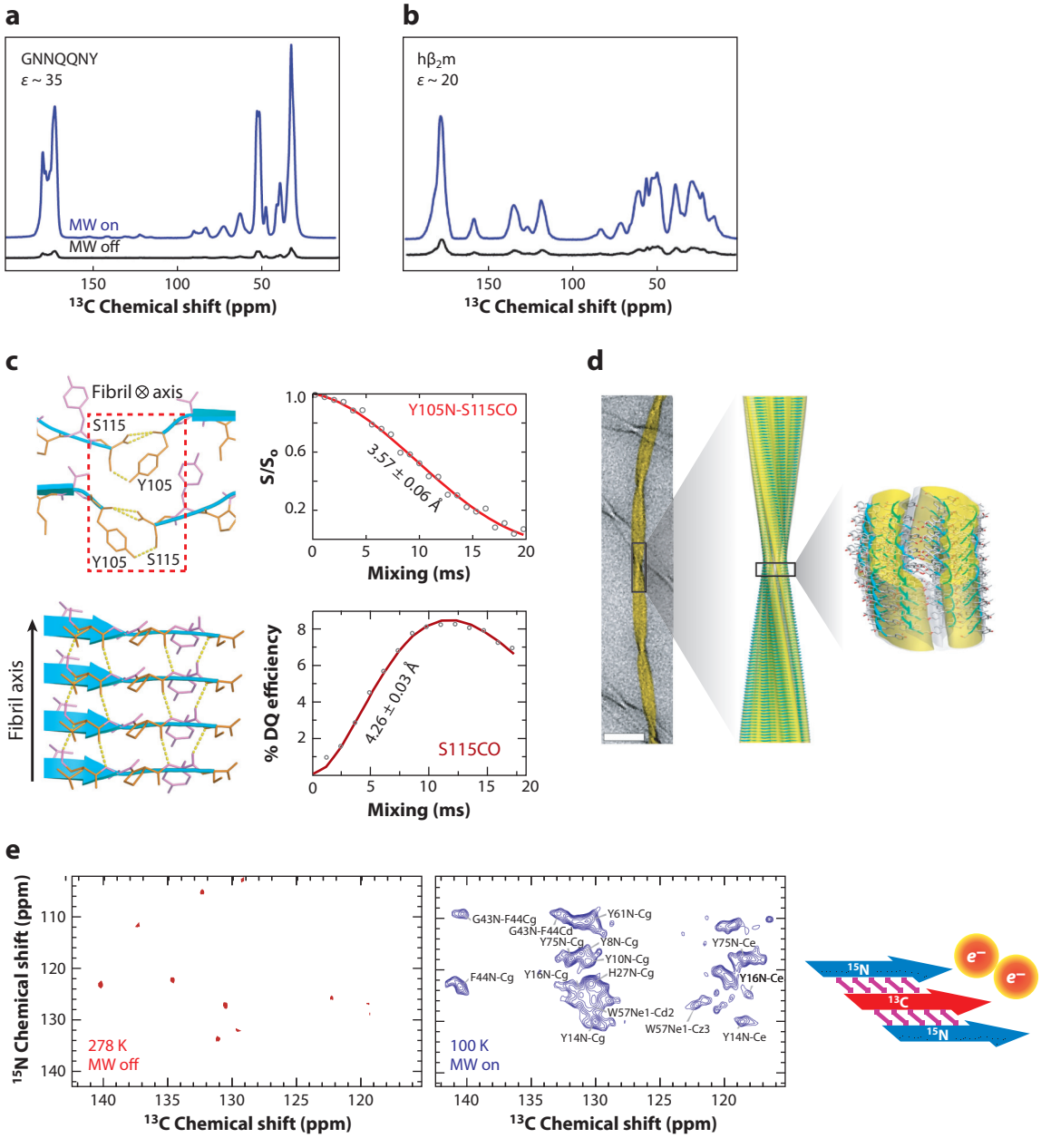

Baldus and colleagues (150) have obtained enhancement factors (ε) of whole cells and cell envelopes with values of 10 and 26, respectively. The spectra revealed NMR signals of integral membrane proteins, lipoproteins, lipids, periplasmic peptidoglycan, and RNAs in uniformly $^{13}C/^{15}N$-labeled whole cells and cell envelopes of *Escherichia coli*, thereby providing a successful example of the characterization of native cellular complexes. $^{1}H/^{13}C/^{15}N$ assignments in the 2D heteronuclear spectra enable the identification of intra- and intermolecular contacts in RNA nucleotides (**Figure 9*a***), which match well with the Watson–Crick base-pairing scheme in RNA bases. Moreover, the overexpressed integral membrane protein PagL has been detected in whole cells using DNP. Interestingly, the average ^{13}C line width is less than 1.0 ppm, which is comparable to line widths in spectra obtained at 271 K.

In addition to the successful DNP-enhanced detection of intracellular components by Renault et al. (150), Hediger and colleagues (146) have characterized cell surfaces of the intact *Bacillus subtilis* bacterial cells. They showed a DNP signal with $\varepsilon = 24$ on extracted cell wall material and whole cells. The polarizing agent TOTAPOL preferentially bound to peptidoglycan, probably via hydrogen bonding, and thus was nonuniformly distributed in the cell walls. The authors used this different binding affinity to selectively enhance or suppress signals of different components in cell walls by adjusting the polarizing agent concentration. The dependence of the enhancement on biradical concentration was demonstrated in 2D DQ and single-quantum (SQ) ^{13}C–^{13}C correlation spectra, which provided ^{13}C assignments of peptidoglycan and the covalently linked wall teichoic acids.

In addition to the phospholipid membrane, many organisms have an extracellular polymorphic layer. As an additional complex to protect against extracellular attack, this layer plays a critical role in all molecular recognition processes. For example, unlike the cells of other eukaryotic organisms, the plant cell has a noncovalent network named the plant cell wall, composed of cellulose, hemicellulose, and pectin, on the outside of the cellular membrane. Cell wall loosening occurs upon interaction with the expansin protein, which enables the cell to grow. The trace amount of expansin in this process and in the noncrystalline plant cell wall has prevented detailed structural characterization. Hong and colleagues (148) recently established the colocalization of expansin and polysaccharides by using DNP. This measurement informs the molecular mechanism responsible for expansin-mediated wall loosening. In their study, an ε value of 27 was achieved in the ^{13}C spectra acquired on a 600-MHz/395-GHz DNP NMR spectrometer at 102 K, allowing NMR observation of the expansin protein in *Arabidopsis* cell wall. Qualitative distances between wild-type and mutated expansins were measured by DNP-enhanced ^{13}C spin diffusion experiments and agree well with the molecular dynamics–simulated model (**Figure 9*b***). These findings have demonstrated that expansin binds to the hemicellulose xyloglucan, resulting in a different structure from that of bulk cellulose.

Figure 8

Representative DNP-enhanced MAS spectra of amyloid fibrils. DNP enhancement of (*a*) GNNQQNY and (*b*) hβ_2m fibrils (112). (*c*) (*Top*) Head-to-tail protofilament arrangement of $TTR_{105-115}$ fibrils constrained by the intermolecular ^{13}C–^{15}N distance between Y105 and S115, measured with DNP-enhanced ^{13}C-^{15}N REDOR. (*Bottom*) Intermolecular distances between the PIR β-strands measured by DNP-enhanced DQF-DRAWS (17, 144). (*d*) The MAS NMR atomic-resolution structure of $TTR_{105-115}$ fibrils fitted into the cryo-EM reconstruction. Intermolecular and interprotofilament distances are quantitatively measured with DNP-enhanced experiments (144). (*e*) Long-mixing ZF-TEDOR spectra (aromatic regions) of the mixed [^{15}N,^{12}C] and [^{14}N,^{13}C] PI3-SH3 fibrils to determine PIR β-strand arrangement (58). Note that many cross-peaks are present in the DNP-enhanced spectrum at 100 K and that there are essentially no signals at 278 K. Abbreviations: DNP, dynamic nuclear polarization; DQF-DRAWS, double quantum filtered dipolar recoupling windowless sequence; EM, electron microscopy; hβ_2m, human β_2 microglobulin; MAS, magic angle spinning; PI3-SH3, the SH3 domain of phosphoinositol 3-kinase; PIR, parallel in register; REDOR, rotational echo double resonance; TTR, transthyretin; ZF-TEDOR, Z-filtered transfer echo double resonance; ε, DNP enhancement.

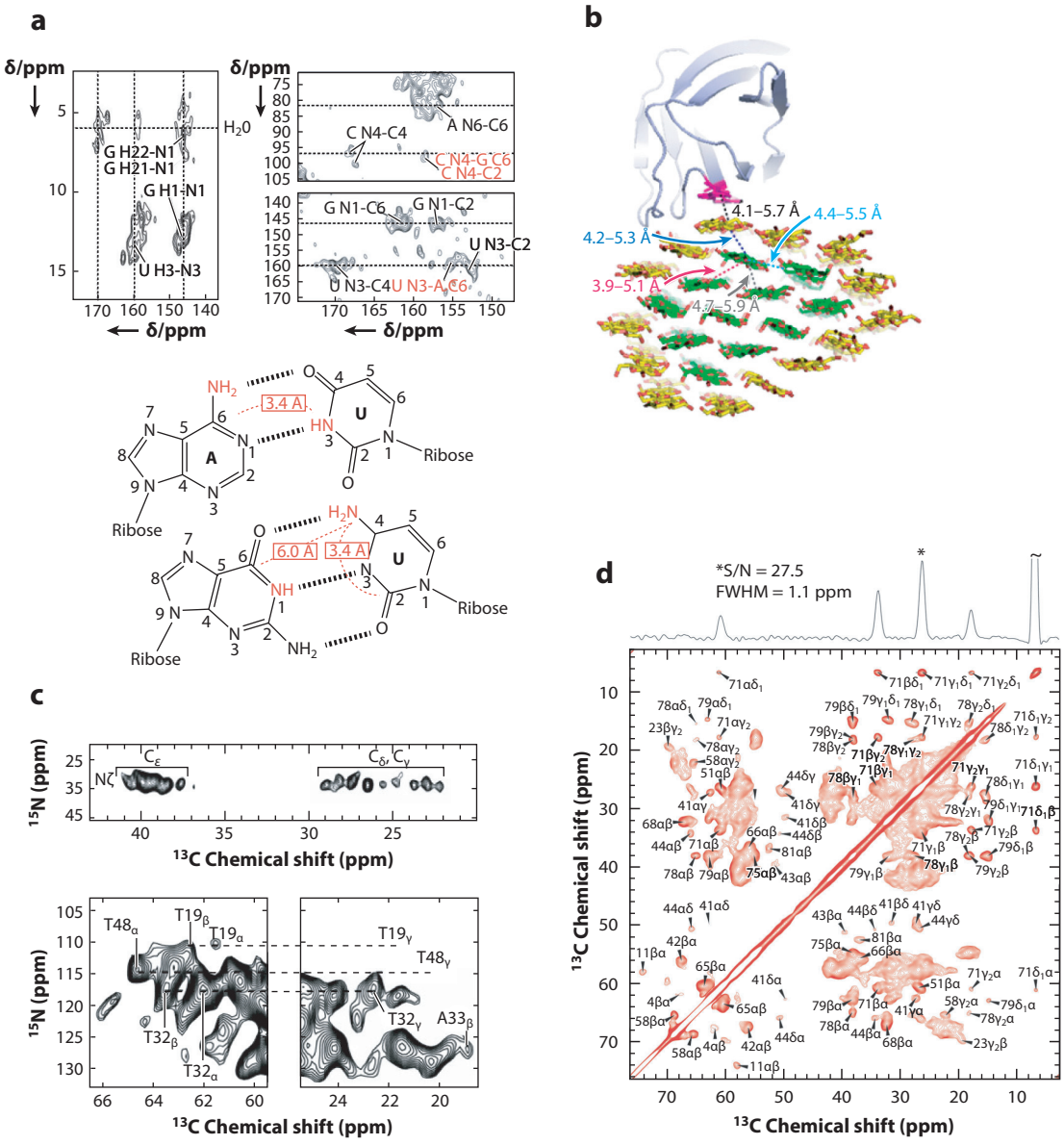

Figure 9

DNP-enhanced SSNMR characterization of various biomacromolecules. (*a*) DNP-enhanced 2D ^{1}H–^{15}N and ^{15}N–^{13}C spectra of uniformly ^{13}C- and ^{15}N-labeled whole cells, showing intra- and intermolecular interactions of RNAs (150). (*b*) The structural model of expansin docking onto a cellulose Iβ microfibril. The distance estimates were obtained from DNP-enhanced ^{1}H spin diffusion experiments (148). (*c*) DNP-enhanced 2D ^{15}N–^{13}C correlation spectra of an 800-kDa ribosome protein, showing a narrow line width (100 Hz for ^{13}C recorded on a 9.4-T spectrometer) (151). The enhancement ($\varepsilon \sim 25$) and resolution enable the assignment of many residues at a cryogenic temperature of 100 K, for example, the threonine and alanine sites. (*d*) The 2D ^{13}C–^{13}C PDSD spectrum of MxiH needles acquired using DNP-enhanced SSNMR at 14.1 T. The spectrum shows an ε value of ~30 and so far is one of the best-resolved 2D spectra at 100 K (155). Abbreviations: DNP, dynamic nuclear polarization; FWHM, full width at half maximum; PDSD, proton-driven spin diffusion; S/N, signal-to-noise ratio; SSNMR, solid-state NMR; 2D, two-dimensional.

Line Width of Frozen Proteins

A concern about the applications of DNP to biological systems involves the line broadening occasionally encountered in the temperature regime from 80 to 100 K. In several cases, involving systems in which the protein is embedded in a well-defined lattice prior to freezing, the resolution is only slightly degraded (**Figure 9**). Examples include bR in its native membrane (10, 32, 33, 98); an 800-kDa ribosomal complex (151); a bacterial type III secretion system (T3SS) needle formed from the MxiH protein (155); neurotoxin bound to acetylcholine receptors in membranes (153); and amyloid fibrils formed from Aβ (162), PI3-SH3 (59), and $TTR_{105-115}$ (144, 156). In the case of bR, the ribosomal complex, and PI3-SH3, the ^{15}N–^{13}C spectra were especially helpful in dispersing cross-peaks and illustrating the width of individual resonances, and the Aβ and T3SS needles exhibited what are currently the best-resolved ^{13}C–^{13}C spectra. Moreover, several nano- and microcrystalline samples exhibited well-ordered structures and narrow line widths at temperatures used for DNP (112, 146, 163–166). In two cases, resolved *J* couplings have been observed at 83 K (163; Q.Z. Ni, E. Markhasin, B. Corzilius, T.V. Can, A.B. Barnes, et al., manuscript submitted).

In contrast to these results, spectra of the small model protein α-spectrin–SH3 dispersed in glassy glycerol/water and examined with ^{13}C–^{13}C proton-driven spin diffusion showed pronounced broadening as the temperature decreased. The line widths in this case were similar to those observed in small molecules dispersed in glassy solvent. Another protein spectrum in which the line widths were broad is that of M2 from influenza A (97). The broadening in these cases likely resulted from conformational distributions that are trapped in the frozen state. For example, a distribution of side-chain orientations may have been frozen in place at low temperatures, causing broadening.

These studies suggest several possible ways to maintain or improve the resolution. First, as is the case with crystallography, it is necessary to develop methods to perform cryoprotection of membranes, amyloids, and other biologically interesting samples. In crystallography, the crystals are small and have little heat capacity, so they can be rapidly frozen in a liquid isopentane or nitrogen. At present, and in contrast, the MAS rotors make up approximately three-quarters of the heat capacity of the sample, so the sample is frozen conductively and slowly as the sample is cooled in the probe. Second, most of the samples employed for DNP have been uniformly ^{13}C labeled, and ^{13}C–^{13}C *J* couplings contribute ~100–150 Hz to the line widths. Thus, sparse labeling with 1,6-$^{13}C_2$-glucose, 2-^{13}C-glucose, 2-^{13}C-glycerol, or 1,3-$^{13}C_2$-glycerol will likely improve the resolution. Another recently introduced sparse labeling approach involves so-called redox labeling with ^{13}C acetate; this approach labels (*a*) 14 amino acids on the side chains in approximately one position and (*b*) the backbone $^{13}C{=}O$ (87) and significantly improves resolution in MAS spectra. Finally, Reif and colleagues (145) have demonstrated that $A\beta_{1-40}$ fibrils exhibit narrow line widths at 100 K that are comparable to those at room temperature. The resolution dramatically increases at higher fields, in particular as recorded on an 850-MHz spectrometer, suggesting that high field is important in circumventing line broadening at temperatures of 80 to 100 K. These advances in sample preparation and instrumentation represent important approaches that will likely further extend applications of DNP NMR to investigations of even larger or more dilute samples.

^1H-Detected Spectra at High Spinning Frequencies

In addition to DNP, ^1H detection of ^{13}C and ^{15}N resonances can also be used to increase the sensitivity of MAS experiments—a strategy, introduced by Bodenhausen & Ruben (12), that is an essential part of most solution NMR experiments. In particular, improvements in MAS rotor

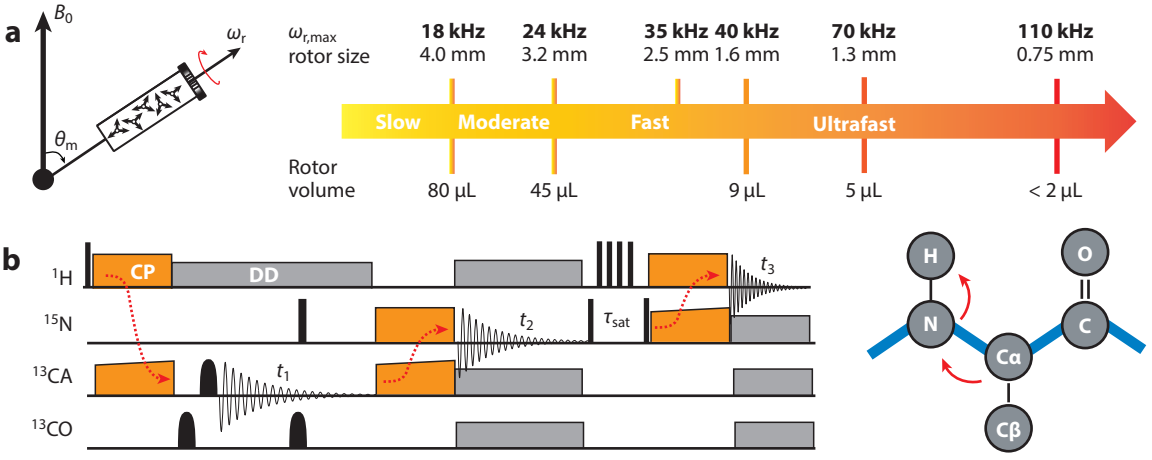
a
B_0
ω_r
θ_m
$\omega_{r,max}$
rotor size
18 kHz
4.0 mm
24 kHz
3.2 mm
35 kHz 40 kHz
2.5 mm 1.6 mm
70 kHz
1.3 mm
110 kHz
0.75 mm
Slow
Moderate
Fast
Ultrafast
Rotor volume
80 µL
45 µL
9 µL
5 µL
< 2 µL
b
^{1}H
^{15}N
^{13}CA
^{13}CO
CP
DD
t_1
t_2
t_3
τ_{sat}
H
N
O
C
Cα
Cβ

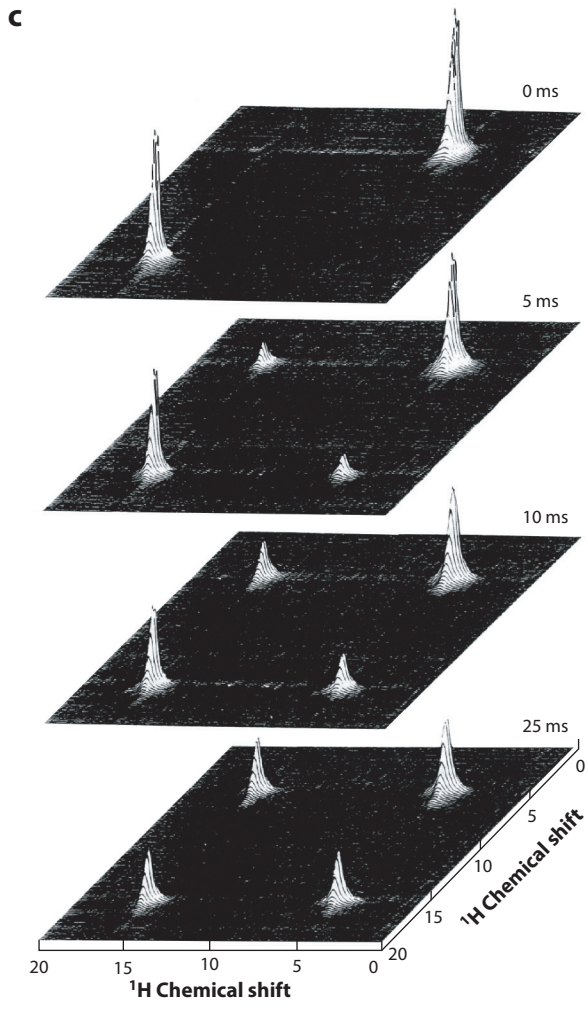
c
0 ms
5 ms
10 ms
25 ms
^{1}H Chemical shift
^{1}H Chemical shift

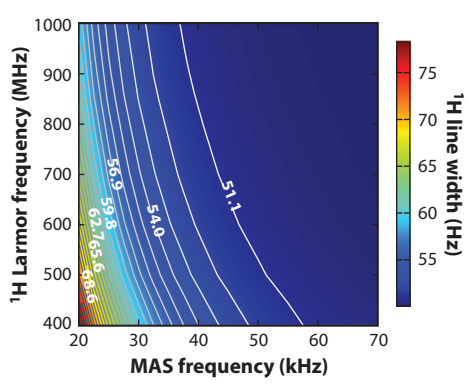
d
^{1}H Larmor frequency (MHz)
MAS frequency (kHz)
^{1}H line width (Hz)
56.9
59.8
62.7
65.6
68.6
54.0
51.1

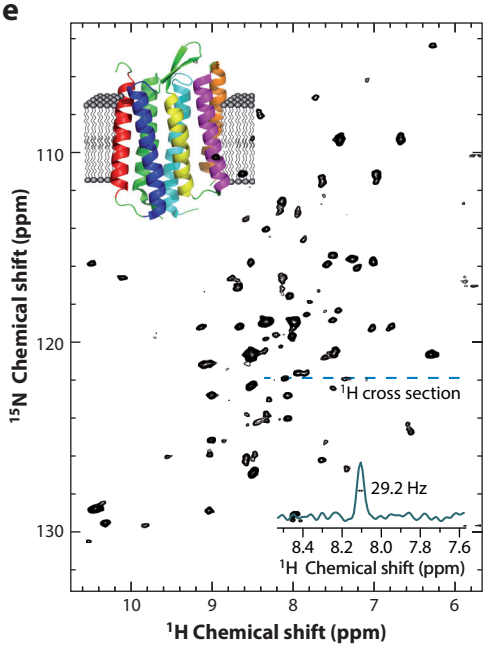
e
^{15}N Chemical shift (ppm)
^{1}H Chemical shift (ppm)
^{1}H cross section
29.2 Hz
^{1}H Chemical shift (ppm)

technology have increased spinning frequencies ($\omega_r/2\pi$) from 10 kHz to >70 kHz, leading to ^{1}H line widths of ~20 Hz for NHs in perdeuterated protein samples, and have yielded an ~30-fold sensitivity increase for ^{15}N detection and an 8–24-fold increase for ^{13}C (13). Although these values are much smaller than the sensitivity increase obtained via DNP, they are still very useful, allowing another spectral dimension to be introduced into MAS experiments. Doing so involves reducing the size of the rotor from 4 mm to 1.3–0.7 mm outer diameter, with a concurrent reduction in sample volume from ~80 μL to 4 μL (**Figure 10*a***). When these spinning frequencies are combined with sample deuteration, they give rise to the possibility of detecting ^{1}H with high resolution and sensitivity (88, 89, 167–174).

Probes equipped for 40–110-kHz MAS are now commercially available from several vendors, and even higher frequency sample spinning is under development. Also, the experiments are most effective at high fields (>18.8 T) because the Zeeman field truncates the ^{1}H–^{1}H flip-flop terms in the dipolar Hamiltonian and permits MAS to narrow the spectrum (135). **Figure 10*b*** shows a typical pulse sequence, (H)CANH, illustrating the implementation of ^{1}H detection; here, ^{1}H is used to cross-polarize Cα, and coherence is transferred to ^{15}N with decoupling of CO, followed by ^{1}H detection.

In 1993, Zheng et al. (175) obtained one of the first high-resolution 2D ^{1}H MAS NMR spectra by utilizing ^{2}H spin dilution to 1% and $\omega_r/2\pi = 10$ kHz (**Figure 10*c***). Whereas most current studies focus on the detection and assignment of resonances, this series of 2D spectra illustrates that it is possible to detect ^{1}H exchange in solids with these experiments. In this case, the process involved a H^+ moving from water to a carboxyl group of oxalic acid. Because many biological processes involve H^+ transfers, the ability to study these processes with MAS NMR leads to interesting possibilities. More recently, ^{1}H detection has been vigorously developed in numerous laboratories (91, 167, 170, 176, 177).

With the presently available spinning frequencies ($\omega_r/2\pi = 60$–70 kHz) and magnetic fields (18.8–23.5 T), investigators typically employ a high degree of sample deuteration to remove the effects of strong ^{1}H–^{1}H dipolar couplings, which are not adequately averaged by MAS. Using $\omega_r/2\pi = 60$ kHz, researchers have achieved high resolution (~20 Hz) with ~100% protein perdeuteration and ~100% back-exchanged ^{1}H at the amide sites. However, an adequate resolution for assignments and many other purposes can be obtained even for full protonation (172, 174). As the available magnetic field is increased, further improvement can be expected given that the higher fields will further truncate the ^{1}H–^{1}H Hamiltonian. Asami et al. (167) recently demonstrated that the proton line width dramatically improves with increased magnetic field and spinning frequency. **Figure 10*c*** shows their reported line widths simulated with varying spinning

Figure 10

^{1}H-detected MAS NMR using high-frequency spinning and proton dilution. (*a*) MAS and the current frequency regime from slow to ultrafast MAS. By spinning solid samples at the magic angle θ_m (~54.74°, where $\cos^2\theta_m = 1/3$) with respect to the direction of B_0, the peak line width can be remarkably narrowed due to the averaging of spin interactions (mainly CSA and dipolar interactions for spin-1/2 nuclei in protein systems). (*b*) A representative ^{1}H-detected pulse sequence, (H)CANH (*left*), and magnetization transfer pathway (*right*) of multidimensional experiments (91). Orange and gray squares donate pulse schemes of CP and DD. (*c*) ^{1}H-detected 2D exchange spectra of 90%-perdeuterated oxalic acid dihydrated at different mixing times. This provided one of the first examples of high-resolution 2D ^{1}H MAS NMR spectra by utilizing deuterium spin dilution. (*d*) Dependence of proton line width on B_0 and on the spinning frequency (167). (*e*) An ^{1}H-detected ^{15}N–^{1}H spectrum of the perdeuterated bR protein in the purple membrane of *Halobacterium salinarium* and a representative ^{1}H cross section (^{1}H FWHM ~ 30 Hz) (168). Abbreviations: B_0, magnetic field; bR, bacteriorhodopsin; CP, cross-polarization; CSA, chemical shift anisotropy; DD, dipolar decoupling; FWHM, full width at half maximum; MAS, magic angle spinning; 2D, two-dimensional.

frequencies and magnetic fields, for a model spin system based on the geometry of lysine. The dramatic improvement in the resolution with increasing magnetic field is evident.

^{1}H-detected MAS NMR techniques have been utilized to investigate several membrane-bound proteins, including bR, OmpG, proteorhodopsin (PR), M2, DsbA, and DsbB (168, 174, 178). The dilution of the ^{1}H network in perdeuterated proteins significantly attenuates the dipolar coupling. This magnetic dilution, together with the efficient homo- and heteronuclear ^{1}H decoupling at $\omega_r/2\pi \geq 60$ kHz, remarkably narrows the peaks. For example, the perdeuterated purple membrane–bound bR protein shows ^{15}N and ^{1}H line widths of 9 and 30 Hz (168), which represent the narrowest lines of membrane proteins in MAS NMR studies to date (**Figure 10*d***). By using a combination of inter- and intramolecular 3D correlation experiments [CANH, CONH, CA(CO)NH, CO(CA)NH, CBCANH, and CBCA(CO)NH], Rienstra and colleagues (174) have successfully completed chemical-shift assignments of the DsbA protein (~27 kDa) in a de novo manner. In the diluted ^{1}H sample, the dipolar truncation of weaker couplings by the stronger ones becomes less important, enabling more efficient detection of long-range ^{1}H correlations. These authors have also shown that the single 2–3-mg perdeuterated DsbA protein sample allows the detection of proton contacts up to 10 Å (174). Proton-detected correlation experiments involving ^{1}H/^{15}N/^{13}C dimensions also permitted the sequential assignment of the solvent-exposed parts of a seven-helical integral membrane proton pump, PR (178).

Barbet-Massin et al. (91) recently demonstrated the utility of ^{1}H detection. In particular, these authors developed a set of six ^{1}H-detected ^{1}H/^{13}C/^{15}N MAS experiments for sequence-specific backbone assignments of MAS spectra and applied them to five proteins in different states, including two microcrystalline proteins, a sedimented virus capsid, and two membrane-embedded systems. As discussed above, this method is based on perdeuteration, amide ^{2}H/^{1}H exchange, 18.8–23.5-T fields, and $\omega_r/2\pi \geq 60$ kHz. These experiments yielded high-quality NMR data that can be automatically analyzed (**Figure 11**). In comparison to contemporary ^{13}C- and ^{15}N-based methods, this approach facilitates and accelerates the MAS NMR assignment process and shortens the spectral acquisition times. We anticipate that this approach will become very useful in MAS NMR studies of proteins. Of course, DNP can easily be integrated into the scheme because, as described, above the optimal approach to performing DNP is to polarize ^{1}H diluted in a ^{2}H lattice such as DNP juice.

CONCLUSIONS AND OUTLOOK

During the past 20 years, the use of MAS NMR of biological systems has expanded dramatically, and this technique is now providing data on many systems that are otherwise unavailable from solution NMR and X-ray diffraction. The limiting factor in expanding the applications for MAS has been its sensitivity, and this article discusses two approaches that are addressing this issue. First, DNP has advanced theoretically and instrumentally and has expanded our understanding of polarization transfer mechanisms, the cryogenic instrumentation and probes required, microwave technology, polarizing agents, and many other aspects. We show that DNP in conjunction with high magnetic fields has developed into a powerful and routine technique to investigate a variety of different biological systems—amyloid fibrils, membrane proteins, ribosomes, and so on. Clearly, the number of these applications is increasing as commercially available instrumentation becomes more widely available. In addition, in the near future it is reasonable to expect the development of new methods to achieve additional gains in sensitivity, for example, methods for electron decoupling and pulsed DNP and more efficient polarizing agents for high-field experiments. Electron decoupling will remove the broadening and intensity loss due to the presence of the paramagnetic polarizing agent, and pulsed DNP methods will circumvent the inverse field dependence exhibited

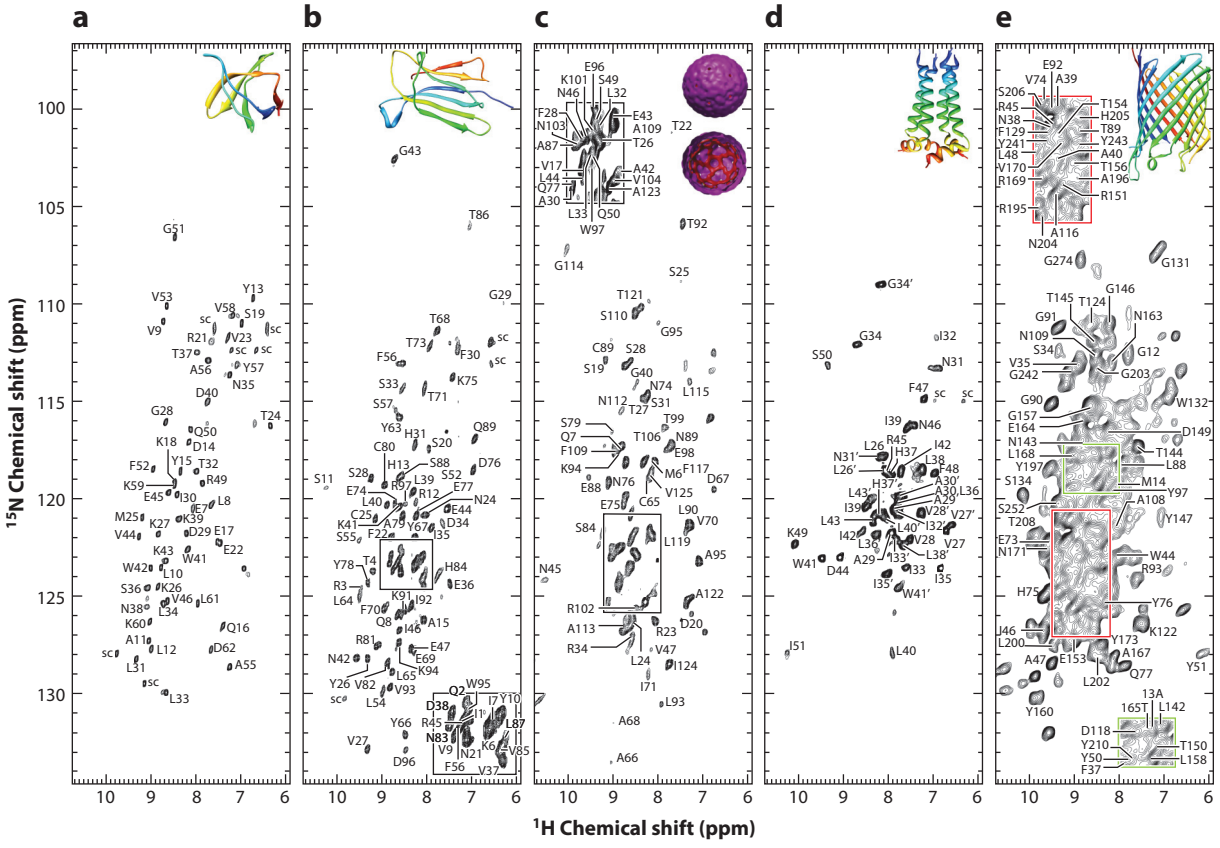

Figure 11

^{15}N–^{1}H correlation spectra recorded on a 1-GHz (23.5-T) spectrometer using a spinning frequency of 60 kHz for five different [UH^{N},^{2}H,^{13}C,^{15}N]-labeled samples. (*a*) Microcrystalline SH3. (*b*) Microcrystalline hβ_2m. (*c*) Sedimented nucleocapsids of AP205. (*d*) The M2$_{18-60}$ channel from influenza A. (*e*) OmpG. Abbreviations: hβ_2m, human β_2 microglobulin; UH^{N}, denotes that the amide protons were fully back-exchanged. Modified from Reference 91.

by CW techniques. New polarizing agents optimized for high fields will enable the full sensitivity of DNP to be realized with increased resolution at high fields.

Second, the advances in instrumentation required for ^{1}H detection—primarily smaller MAS rotors that will spin at higher rates—are much simpler and less sophisticated than those for DNP. These rotors are now available and are being used in a variety of applications. Approaches to ^{1}H detection will utilize many properties that are now well understood for MAS and solution NMR experiments, such as cross-polarization and *J*-mediated transfers. Although the sensitivity enhancements are much smaller than those available from DNP, they are nevertheless significant. Finally, as discussed above, we anticipate that DNP and ^{1}H detection will likely merge into a single experimental approach, further expanding the applicability of MAS NMR to biological systems.

DISCLOSURE STATEMENT

The authors are not aware of any affiliations, memberships, funding, or financial holdings that might be perceived as affecting the objectivity of this review.

LITERATURE CITED

1. Comellas G, Rienstra CM. 2013. Protein structure determination by magic-angle spinning solid-state NMR, and insights into the formation, structure, and stability of amyloid fibrils. *Annu. Rev. Biophys.* 42:515–36
2. Hong M, Zhang Y, Hu F. 2012. Membrane protein structure and dynamics from NMR spectroscopy. *Annu. Rev. Phys. Chem.* 63:1–24
3. McDermott A. 2009. Structure and dynamics of membrane proteins by magic angle spinning solid-state NMR. *Annu. Rev. Biophys.* 38:385–403
4. Yan S, Suiter CL, Hou G, Zhang H, Polenova T. 2013. Probing structure and dynamics of protein assemblies by magic angle spinning NMR spectroscopy. *Acc. Chem. Res.* 46:2047–58
5. Tycko R. 2011. Solid-state NMR studies of amyloid fibril structure. *Annu. Rev. Phys. Chem.* 62:279–99
6. Weingarth M, Baldus M. 2013. Solid-state NMR-based approaches for supramolecular structure elucidation. *Acc. Chem. Res.* 46:2037–46
7. Barnes AB, De Paëpe G, van der Wel PC, Hu KN, Joo CG, et al. 2008. High-field dynamic nuclear polarization for solid and solution biological NMR. *Appl. Magn. Reson.* 34:237–63
8. Cheng CY, Han S. 2013. Dynamic nuclear polarization methods in solids and solutions to explore membrane proteins and membrane systems. *Annu. Rev. Phys. Chem.* 64:507–32
9. Ni QZ, Daviso E, Can TV, Markhasin E, Jawla SK, et al. 2013. High frequency dynamic nuclear polarization. *Acc. Chem. Res.* 46:1933–41
10. Mak-Jurkauskas ML, Bajaj VS, Hornstein MK, Belenky M, Griffin RG, Herzfeld J. 2008. Energy transformations early in the bacteriorhodopsin photocycle revealed by DNP-enhanced solid-state NMR. *PNAS* 105:883–88
11. Hu KN. 2011. Polarizing agents and mechanisms for high-field dynamic nuclear polarization of frozen dielectric solids. *Solid State Nucl. Magn. Reson.* 40:31–41
12. Bodenhausen G, Ruben DJ. 1980. Natural abundance nitrogen-15 NMR by enhanced heteronuclear spectroscopy. *Chem. Phys. Lett.* 69:185–89
13. Bax A, Sparks SW, Torchia DA. 1989. Detection of insensitive nuclei. *Methods Enzymol.* 176:134–50
14. Knight MJ, Pell AJ, Bertini I, Felli IC, Gonnelli L, et al. 2012. Structure and backbone dynamics of a microcrystalline metalloprotein by solid-state NMR. *PNAS* 109:11095–100
15. Nieuwkoop AJ, Wylie BJ, Franks WT, Shah GJ, Rienstra CM. 2009. Atomic resolution protein structure determination by three-dimensional transferred echo double resonance solid-state nuclear magnetic resonance spectroscopy. *J. Chem. Phys.* 131:095101
16. Shahid SA, Bardiaux B, Franks WT, Krabben L, Habeck M, et al. 2012. Membrane protein structure determination by solid-state NMR spectroscopy of microcrystals. *Nat. Methods* 9:1212–17
17. Fitzpatrick AW, Debelouchina GT, Bayro MJ, Clare DK, Caporini MA, et al. 2013. Atomic structure and hierarchical assembly of a cross-β-amyloid fibril. *PNAS* 110:5468–73
18. Lu GJ, Tian Y, Vora N, Marassi FM, Opella SJ. 2013. The structure of the mercury transporter MerF in phospholipid bilayers: A large conformational rearrangement results from N-terminal truncation. *J. Am. Chem. Soc.* 135:9299–302
19. Lu J-X, Qiang W, Yau W-M, Schwieters CD, Meredith SC, Tycko R. 2013. Molecular structure of β-amyloid fibrils in Alzheimer's disease brain tissue. *Cell* 154:1257–68
20. Hong M, Su Y. 2011. Structure and dynamics of cationic membrane peptides and proteins: insights from solid-state NMR. *Protein Sci.* 20:641–55
21. Andreas LB, Eddy MT, Chou JJ, Griffin RG. 2012. Magic-angle-spinning NMR of the drug resistant S31N M2 proton transporter from influenza A. *J. Am. Chem. Soc.* 134:7215–18
22. Wang S, Munro RA, Shi L, Kawamura I, Okitsu T, et al. 2013. Solid-state NMR spectroscopy structure determination of a lipid-embedded heptahelical membrane protein. *Nat. Methods* 10:1007–12
23. Oldfield E. 1973. Are cell membranes fluid? *Science* 180:982–83
24. Singer SJ, Nicolson GL. 1972. The fluid mosaic model of the structure of cell membranes. *Science* 175:720–31
25. Starling AP, East JM, Lee AG. 1995. Effects of gel phase phospholipid on the Ca^{2+}-ATPase. *Biochemistry* 34:3084–91

26. Debelouchina GT, Platt GW, Bayro MJ, Radford SE, Griffin RG. 2010. Intermolecular alignment in β_2-microglobulin amyloid fibrils. *J. Am. Chem. Soc.* 132:17077–79
27. Wasmer C, Lange A, Van Melckebeke H, Siemer AB, Riek R, Meier BH. 2008. Amyloid fibrils of the HET-$s_{218-289}$ prion form a β solenoid with a triangular hydrophobic core. *Science* 319:1523–26
28. Su Y, Sarell CJ, Eddy MT, Debelouchina GT, Andreas LB, et al. 2014. Secondary structure in the core of amyloid fibrils formed from human β_2m and its truncated variant ΔN6. *J. Am. Chem. Soc.* 136:6313–25
29. Almén MS, Nordström KJ, Fredriksson R, Schiöth HB. 2009. Mapping the human membrane proteome: A majority of the human membrane proteins can be classified according to function and evolutionary origin. *BMC Biol.* 7:50
30. Su Y, Li S, Hong M. 2013. Cationic membrane peptides: atomic-level insight of structure–activity relationships from solid-state NMR. *Amino Acids* 44:821–33
31. Zhou HX, Cross TA. 2013. Influences of membrane mimetic environments on membrane protein structures. *Annu. Rev. Biophys.* 42:361–92
32. Bajaj VS, Mak-Jurkauskas ML, Belenky M, Herzfeld J, Griffin RG. 2009. Functional and shunt states of bacteriorhodopsin resolved by 250 GHz dynamic nuclear polarization–enhanced solid-state NMR. *PNAS* 106:9244–49
33. Bajaj VS, Mak-Jurkauskas ML, Belenky M, Herzfeld J, Griffin RG. 2010. DNP enhanced frequency selective TEDOR experiments in bacteriorhodopsin. *J. Magn. Reson.* 202:9–13
34. Ladizhansky V. 2014. Recent advances in magic-angle spinning solid-state NMR of proteins. *Israel J. Chem.* 54:86–103
35. Bhate MP, Wylie BJ, Tian L, McDermott AE. 2010. Conformational dynamics in the selectivity filter of KcsA in response to potassium ion concentration. *J. Mol. Biol.* 401:155–66
36. Varga K, Tian L, McDermott AE. 2007. Solid-state NMR study and assignments of the KcsA potassium ion channel of *S. lividans*. *Biochim. Biophys. Acta* 1774:1604–13
37. Eddy MT, Ong TC, Clark L, Teijido O, van der Wel PC, et al. 2012. Lipid dynamics and protein–lipid interactions in 2D crystals formed with the β-barrel integral membrane protein VDAC1. *J. Am. Chem. Soc.* 134:6375–87
38. Park SH, Das BB, Casagrande F, Tian Y, Nothnagel HJ, et al. 2012. Structure of the chemokine receptor CXCR1 in phospholipid bilayers. *Nature* 491:779–83
39. Tang M, Comellas G, Rienstra CM. 2013. Advanced solid-state NMR approaches for structure determination of membrane proteins and amyloid fibrils. *Acc. Chem. Res.* 46:2080–88
40. Cross TA, Dong H, Sharma M, Busath DD, Zhou HX. 2012. M2 protein from influenza A: from multiple structures to biophysical and functional insights. *Curr. Opin. Virol.* 2:128–33
41. Andreas LB, Eddy MT, Pielak RM, Chou J, Griffin RG. 2010. Magic angle spinning NMR investigation of influenza A $M2_{18-60}$: support for an allosteric mechanism of inhibition. *J. Am. Chem. Soc.* 132:10958–60
42. Chiti F, Dobson CM. 2006. Protein misfolding, functional amyloid, and human disease. *Annu. Rev. Biochem.* 75:333–66
43. Sipe JD, Cohen AS. 2000. Review: History of the amyloid fibril. *J. Struct. Biol.* 130:88–98
44. Barnhart MM, Chapman MR. 2006. Curli biogenesis and function. *Annu. Rev. Microbiol.* 60:131–47
45. White HE, Hodgkinson JL, Jahn TR, Cohen-Krausz S, Gosal WS, et al. 2009. Globular tetramers of β_2-microglobulin assemble into elaborate amyloid fibrils. *J. Mol. Biol.* 389:48–57
46. Sarell CJ, Woods LA, Su Y, Debelouchina GT, Ashcroft AE, et al. 2013. Expanding the repertoire of amyloid polymorphs by co-polymerization of related protein precursors. *J. Biol. Chem.* 288:7327–37
47. Lansbury PT, Costa PR, Griffiths JM, Simon EJ, Auger M, et al. 1995. Structural model for the β-amyloid fibril: interstrand alignment of an antiparallel β-sheet comprising a C-terminal peptide. *Nat. Struct. Biol.* 2:990–98
48. Benzinger TLS, Gregory DM, Burkoth TS, Miller-Auer H, Lynn DG, et al. 2000. Two-dimensional structure of β-$amyloid_{10-35}$ fibrils. *Biochemistry* 39:3491–99
49. Balbach JJ, Ishii Y, Antzutkin ON, Leapman RD, Rizzo NW, et al. 2000. Amyloid fibril formation by $A\beta_{16-22}$, a seven-residue fragment of the Alzheimer's β-amyloid peptide, and structural characterization by solid state NMR. *Biochemistry* 39:13748–59

50. Heise H, Hoyer W, Becker S, Andronesi OC, Riedel D, Baldus M. 2005. Molecular-level secondary structure, polymorphism, and dynamics of full-length α-synuclein fibrils studied by solid-state NMR. *PNAS* 102:15871–76
51. Comellas G, Lemkau LR, Nieuwkoop AJ, Kloepper KD, Ladror DT, et al. 2011. Structured regions of α-synuclein fibrils include the early-onset Parkinson's disease mutation sites. *J. Mol. Biol.* 411:881–95
52. Lv G, Kumar A, Giller K, Orcellet ML, Riedel D, et al. 2012. Structural comparison of mouse and human α-synuclein amyloid fibrils by solid-state NMR. *J. Mol. Biol.* 420:99–111
53. Luckgei N, Schütz AK, Bousset L, Habenstein B, Sourigues Y, et al. 2013. The conformation of the prion domain of Sup35p in isolation and in the full-length protein. *Angew. Chem. Int. Ed.* 52:12741–44
54. Shewmaker F, Wickner RB, Tycko R. 2006. Amyloid of the prion domain of Sup35p has an in-register parallel β-sheet structure. *PNAS* 103:19754–59
55. Helmus JJ, Surewicz K, Surewicz WK, Jaroniec CP. 2010. Conformational flexibility of Y145Stop human prion protein amyloid fibrils probed by solid-state nuclear magnetic resonance spectroscopy. *J. Am. Chem. Soc.* 132:2393–403
56. Debelouchina GT, Bayro MJ, van der Wel PC, Caporini MA, Barnes AB, et al. 2010. Dynamic nuclear polarization-enhanced solid-state NMR spectroscopy of GNNQQNY nanocrystals and amyloid fibrils. *Phys. Chem. Chem. Phys.* 12:5911–19
57. Debelouchina GT, Platt GW, Bayro MJ, Radford SE, Griffin RG. 2010. Magic angle spinning NMR analysis of β_2-microglobulin amyloid fibrils in two distinct morphologies. *J. Am. Chem. Soc.* 132:10414–23
58. Bayro MJ, Debelouchina GT, Eddy MT, Birkett NR, MacPhee CE, et al. 2011. Intermolecular structure determination of amyloid fibrils with magic-angle spinning and dynamic nuclear polarization NMR. *J. Am. Chem. Soc.* 133:13967–74
59. Bayro MJ, Maly T, Birkett NR, MacPhee CE, Dobson CM, Griffin RG. 2010. High-resolution MAS NMR analysis of PI3-SH3 amyloid fibrils: backbone conformation and implications for protofilament assembly and structure. *Biochemistry* 49:7474–84
60. Reichhardt C, Cegelski L. 2014. Solid-state NMR for bacterial biofilms. *Mol. Phys.* 112:887–94
61. McCrate OA, Zhou X, Reichhardt C, Cegelski L. 2013. Sum of the parts: composition and architecture of the bacterial extracellular matrix. *J. Mol. Biol.* 425:4286–94
62. Shewmaker F, McGlinchey RP, Thurber KR, McPhie P, Dyda R, et al. 2009. The functional curli amyloid is not based on in-register parallel β-sheet structure. *J. Biol. Chem.* 284:25065–76
63. Tycko R, Wickner RB. 2013. Molecular structures of amyloid and prion fibrils: consensus versus controversy. *Acc. Chem. Res.* 46:1487–96
64. Mishra R, Hoop CL, Kodali R, Sahoo B, van der Wel PC, Wetzel R. 2012. Serine phosphorylation suppresses huntingtin amyloid accumulation by altering protein aggregation properties. *J. Mol. Biol.* 424:1–14
65. De Paëpe G, Lewandowski JR, Loquet A, Böckmann A, Griffin RG. 2008. Proton assisted recoupling and protein structure determination. *J. Chem. Phys.* 129:245101
66. De Paëpe G, Lewandowski J, Loquet A, Eddy M, Megy S, et al. 2011. Heteronuclear proton assisted recoupling. *J. Chem. Phys.* 134:095101
67. Lewandowski JR, De Paëpe G, Eddy MT, Griffin RG. 2009. ^{15}N–^{15}N proton assisted recoupling in magic angle spinning NMR. *J. Am. Chem. Soc.* 131:5769–76
68. Lewandowski JR, De Paëpe G, Eddy MT, Struppe J, Maas W, Griffin RG. 2009. Proton assisted recoupling at high spinning frequencies. *J. Phys. Chem. B* 113:9062–69
69. Lewandowski JR, De Paëpe G, Griffin RG. 2007. Proton assisted insensitive nuclei cross polarization. *J. Am. Chem. Soc.* 129:728–29
70. De Paëpe G. 2012. Dipolar recoupling in magic angle spinning solid-state nuclear magnetic resonance. *Annu. Rev. Phys. Chem.* 63:661–84
71. Scholz I, Huber M, Manolikas T, Meier BH, Ernst M. 2008. MIRROR recoupling and its application to spin diffusion under fast magic-angle spinning. *Chem. Phys. Lett.* 460:278–83
72. Weingarth M, Bodenhausen G, Tekely P. 2009. Broadband carbon-13 correlation spectra of microcrystalline proteins in very high magnetic fields. *J. Am. Chem. Soc.* 131:13937–39

73. Hou G, Yan S, Sun S, Han Y, Byeon IJ, et al. 2011. Spin diffusion driven by R-symmetry sequences: applications to homonuclear correlation spectroscopy in MAS NMR of biological and organic solids. *J. Am. Chem. Soc.* 133:3943–53
74. Elena B, Lesage A, Steuernagel S, Böckmann A, Emsley L. 2005. Proton to carbon-13 INEPT in solid-state NMR spectroscopy. *J. Am. Chem. Soc.* 127:17296–302
75. Chen L, Kaiser JM, Polenova T, Yang J, Rienstra CM, Mueller LJ. 2007. Backbone assignments in solid-state proteins using *J*-based 3D heteronuclear correlation spectroscopy. *J. Am. Chem. Soc.* 129:10650–51
76. Nadaud PS, Helmus JJ, Kall SL, Jaroniec CP. 2009. Paramagnetic ions enable tuning of nuclear relaxation rates and provide long-range structural restraints in solid-state NMR of proteins. *J. Am. Chem. Soc.* 131:8108–20
77. Su Y, Hu F, Hong M. 2012. Paramagnetic Cu(II) for probing membrane protein structure and function: inhibition mechanism of the influenza M2 proton channel. *J. Am. Chem. Soc.* 134:8693–702
78. Su Y, Mani R, Hong M. 2008. Asymmetric insertion of membrane proteins in lipid bilayers by solid-state NMR paramagnetic relaxation enhancement: a cell-penetrating peptide example. *J. Am. Chem. Soc.* 130:8856–64
79. Sengupta I, Nadaud PS, Jaroniec CP. 2013. Protein structure determination with paramagnetic solid-state NMR spectroscopy. *Acc. Chem. Res.* 46:2117–26
80. Matsuki Y, Eddy MT, Herzfeld J. 2009. Spectroscopy by integration of frequency and time domain information (SIFT) for fast acquisition of high resolution dark spectra. *J. Am. Chem. Soc.* 131:4648–56
81. Matsuki Y, Eddy MT, Griffin RG, Herzfeld J. 2010. Rapid 3D MAS NMR spectroscopy at critical sensitivity. *Angew. Chem. Int. Ed.* 49:1–5
82. Paramasivam S, Suiter CL, Hou G, Sun S, Palmer M, et al. 2012. Enhanced sensitivity by nonuniform sampling enables multidimensional MAS NMR spectroscopy of protein assemblies. *J. Phys. Chem. B* 116:7416–27
83. Laage S, Sachleben JR, Steuernagel S, Pierattelli R, Pintacuda G, Emsley L. 2009. Fast acquisition of multi-dimensional spectra in solid-state NMR enabled by ultra-fast MAS. *J. Magn. Reson.* 196:133–41
84. Hong M, Jakes K. 1999. Selective and extensive ^{13}C labeling of a membrane protein for solid-state NMR investigations. *J. Biomol. NMR* 14:71–74
85. Lundström P, Teilum K, Carstensen T, Bezsonova I, Wiesner S, et al. 2007. Fractional ^{13}C enrichment of isolated carbons using [1-^{13}C]- or [2-^{13}C]-glucose facilitates the accurate measurement of dynamics at backbone C^{α} and side-chain methyl positions in proteins. *J. Biomol. NMR* 38:199–212
86. Higman VA, Flinders J, Hiller M, Jehle S, Markovic S, et al. 2009. Assigning large proteins in the solid state: a MAS NMR resonance assignment strategy using selectively and extensively ^{13}C-labelled proteins. *J. Biomol. NMR* 44:245–60
87. Eddy MT, Belenky M, Sivertsen A, Griffin RG, Herzfeld J. 2013. Selectively dispersed isotope labeling for protein structure determination by magic angle spinning NMR. *J. Biomol. NMR* 57:129–39
88. Knight MJ, Webber AL, Pell AJ, Guerry P, Barbet-Massin E, et al. 2011. Fast resonance assignment and fold determination of human superoxide dismutase by high-resolution proton-detected solid-state MAS NMR spectroscopy. *Angew. Chem. Int. Ed.* 50:11697–701
89. Huber M, Hiller S, Schanda P, Ernst M, Böckmann A, et al. 2011. A proton-detected 4D solid-state NMR experiment for protein structure determination. *ChemPhysChem* 12:915–18
90. Zhou D, Shea J, Nieuwkoop A, Franks W, Wylie B, et al. 2007. Solid-state protein-structure determination with proton-detected triple-resonance 3D magic-angle-spinning NMR spectroscopy. *Angew. Chem. Int. Ed.* 46:8380–83
91. Barbet-Massin E, Pell AJ, Retel JS, Andreas LB, Jaudzems K, et al. 2014. Rapid proton-detected NMR assignment for proteins with fast magic angle spinning. *J. Am. Chem. Soc.* 136:12489–97
92. Moms GA, Freeman R. 1979. Enhancement of nuclear magnetic resonance signals by polarization transfer. *J. Am. Chem. Soc.* 101:760–62
93. Pines A, Gibby MG, Waugh JS. 1973. Proton-enhanced NMR of dilute spins in solids. *J. Chem. Phys.* 59:569–90
94. Hu KN, Song C, Yu HH, Swager TM, Griffin RG. 2008. High-frequency dynamic nuclear polarization using biradicals: a multifrequency EPR lineshape analysis. *J. Chem. Phys.* 128:052302

95. Ernst RR, Bodenhausen G, Wokaun A. 1991. *Principles of Nuclear Magnetic Resonance in One and Two Dimensions*. Oxford, UK: Clarendon
96. Sauvée C, Rosay M, Casano G, Aussenac F, Weber RT, et al. 2013. Highly efficient, water-soluble polarizing agents for dynamic nuclear polarization at high frequency. *Angew. Chem. Int. Ed.* 52:10858–61
97. Andreas LB, Barnes AB, Corzilius B, Chou JJ, Miller EA, et al. 2013. Dynamic nuclear polarization study of inhibitor binding to the $M2_{18-60}$ proton transporter from influenza A. *Biochemistry* 52:2774–82
98. Barnes A, Corzilius B, Mak-Jurkauskas M, Andreas L, Bajaj V, et al. 2010. Resolution and polarization distribution in cryogenic DNP/MAS experiments. *Phys. Chem. Chem. Phys.* 12:5861–67
99. Overhauser AW. 1953. Polarization of nuclei in metals. *Phys. Rev.* 92:411
100. Carver TR, Slichter CP. 1956. Experimental verification of the Overhauser nuclear polarization effect. *Phys. Rev.* 102:975–80
101. Barnes AB, Nanni EA, Herzfeld J, Griffin RG, Temkin RJ. 2012. A 250 GHz gyrotron with a 3 GHz tuning bandwidth for dynamic nuclear polarization. *J. Magn. Reson.* 221:147–53
102. Abragam A, Goldman M. 1978. Principles of dynamic nuclear polarization. *Rep. Prog. Phys.* 41:395–467
103. Atsarkin VA. 1978. Dynamic polarization of nuclei in solid dielectrics. *Soviet Phys. Solid State* 21:725–44
104. Jefferies CD. 1957. Polarization of nuclei by resonance saturation in paramagnetic crystals. *Phys. Rev.* 106:164–65
105. Jefferies CD. 1960. Dynamic orientation of nuclei by forbidden transitions in paramagnetic resonance. *Phys. Rev.* 117:1056–69
106. Abragam A, Proctor WG. 1958. Une nouvelle méthode de polarisation dynamique des noyaux atomiques dans les solides. *C. R. Hebd. Séances Acad. Sci.* 246:2253–56
107. Kessenikh AV, Luschikov VL, Manenkov AA, Taran YV. 1963. Proton polarization in irradiated polyethylenes. *Soviet Phys. Solid State* 5:321–29
108. Kessenikh AV, Manenkov AA. 1963. Dynamic polarization of nuclei during saturation of nonuniformly broadened electron paramagnetic resonance lines. *Soviet Phys. Solid State* 5:835–37
109. Kessenikh AV, Manenkov AA, Pyatnitskii GI. 1964. On explanation of experimental data on dynamic polarization of protons in irradiated polyethylenes. *Soviet Phys. Solid State* 6:641–43
110. Wind RA, Duijvestijn MJ, Van der Lugt C, Manenschijn A, Vriend J. 1985. Applications of dynamic nuclear polarization in ^{13}C NMR in solids. *Prog. Nucl. Magn. Reson. Spectrosc.* 17:33–67
111. Hausser KH, Stehlik D. 1968. Dynamic nuclear polarization in liquids. *Adv. Magn. Reson.* 3:79–139
112. van der Wel PC, Hu KN, Lewandowski J, Griffin R. 2006. Dynamic nuclear polarization of amyloidogenic peptide nanocrystals: GNNQQNY, a core segment of the yeast prion protein Sup35p. *J. Am. Chem. Soc.* 128:10840–46
113. Smith AA, Corzilius B, Barnes AB, Maly T, Griffin RG. 2012. Solid effect dynamic nuclear polarization and polarization pathways. *J. Chem. Phys.* 136:015101
114. Singel DJ, Seidel H, Kendrick RD, Yannoni CS. 1989. A spectrometer for EPR, DNP, and multinuclear high-resolution NMR. *J. Magn. Reson.* 81:145–61
115. Afeworki M, McKay RA, Schaefer J. 1992. Selective observation of the interface of heterogeneous polycarbonate/polystyrene blends by dynamic nuclear polarization carbon-13 NMR spectroscopy. *Macromolecules* 25:4084–91
116. Becerra LR, Gerfen GJ, Temkin RJ, Singel DL, Griffin RG. 1993. Dynamic nuclear polarization with a cyclotron resonance maser at 5 T. *Phys. Rev. Lett.* 71:3561–64
117. Gerfen GJ, Becerra LR, Hall DA, Griffin RG, Temkin RJ, Singel DJ. 1995. High frequency (140 GHz) dynamic nuclear polarization: polarization transfer to a solute in frozen aqueous solution. *J. Chem. Phys.* 102:9494–97
118. Nanni EA, Barnes AB, Griffin RG, Temkin RJ. 2011. THz dynamic nuclear polarization NMR. *IEEE Trans. Terahertz Sci. Technol.* 1:145–63
119. Allen PJ, Creuzet F, De Groot HJM, Griffin RG. 1991. Apparatus for low-temperature magic-angle spinning NMR. *J. Magn. Reson.* 92:614–17
120. Barnes AB, Mak-Jurkauskas ML, Matsuki Y, Bajaj VS, van der Wel PC, et al. 2009. Cryogenic sample exchange NMR probe for magic angle spinning dynamic nuclear polarization. *J. Magn. Reson.* 198:261–70

121. Woskov PW, Bajaj VS, Hornstein MK, Temkin RJ, Griffin RG. 2005. Corrugated waveguide and directional coupler for CW 250 GHz gyrotron DNP experiments. *IEEE Trans. Microw. Theory Tech.* 53:1863–69
122. Hu KN, Yu H-H, Swager TM, Griffin RG. 2004. Dynamic nuclear polarization with biradicals. *J. Am. Chem. Soc.* 126:10844–45
123. Hu KN, Bajaj VS, Rosay M, Griffin RG. 2007. High-frequency dynamic nuclear polarization using mixtures of TEMPO and trityl radicals. *J. Chem. Phys.* 126:044512
124. Wollan DS. 1976. Dynamic nuclear polarization with an inhomogeneously broadened ESR line. I. Theory. *Phys. Rev. B* 13:3671
125. Maly T, Debelouchina GT, Bajaj VS, Hu KN, Joo CG, et al. 2008. Dynamic nuclear polarization at high magnetic fields. *J. Chem. Phys.* 128:052211
126. Haze O, Corzilius B, Smith AA, Griffin RG, Swager TM. 2012. Water-soluble narrow-line radicals for dynamic nuclear polarization. *J. Am. Chem. Soc.* 134:14287–90
127. Can TV, Caporini MA, Mentink-Vigier F, Corzilius B, Walish JJ, et al. 2014. Overhauser effects in insulating solids. *J. Chem. Phys.* 141:064202
128. Hu KN, Debelouchina GT, Smith AA, Griffin RG. 2011. Quantum mechanical theory of dynamic nuclear polarization in solid dielectrics. *J. Chem. Phys.* 134:125105
129. Hu KN, Song C, Yu H-H, Swager TM, Griffin RG. 2008. High-frequency dynamic nuclear polarization using biradicals: a multifrequency EPR lineshape analysis. *J. Chem. Phys.* 128:052321
130. Thurber K, Tycko R. 2012. Theory for cross effect dynamic nuclear polarization under magic angle spinning in solid state nuclear magnetic resonance: the importance of level crossings. *J. Chem. Phys.* 137:084508
131. Hovav Y, Feintuch A, Vega S. 2010. Theoretical aspects of dynamic nuclear polarization in the solid state—the solid effect. *J. Magn. Reson.* 207:176–89
132. Mentink-Vigier F, Akbey Ü, Hovav Y, Vega S, Oschkinat H, Feintuch A. 2013. Fast passage dynamic nuclear polarization on rotating solids. *J. Magn. Reson.* 224:13–21
133. Mak-Jurkauskas ML, Griffin RG. 2007. High-frequency dynamic nuclear polarization. In *Solid-State NMR of Biopolymers*, ed. AE McDermott, T Polenova, pp. 159–74. New York: Wiley
134. Maricq MM, Waugh JS. 1977. Rotational spin echoes and high resolution NMR in powders. *Chem. Phys. Lett.* 47:327–29
135. Maricq MM, Waugh JS. 1979. NMR in rotating solids. *J. Chem. Phys.* 70:3300–16
136. Matsuki Y, Maly T, Ouari O, Karoui H, Le Moigne F, et al. 2009. Dynamic nuclear polarization with a rigid biradical. *Angew. Chem. Int. Ed.* 48:4996–5000
137. Song C, Hu KN, Joo C-G, Swager TM, Griffin RG. 2006. TOTAPOL—a biradical polarizing agent for dynamic nuclear polarization experiments in aqueous media. *J. Am. Chem. Soc.* 128:11385–90
138. La Mar GN, Horrocks WD, Holm RH. 1973. *NMR of Paramagnetic Molecules: Principles and Applications*. San Diego: Academic
139. Satterlee JD. 1990. Fundamental concepts of NMR in paramagnetic systems. Part II: Relaxation phenomena. *Concepts Magn. Res.* 2:119–29
140. Corzilius B, Andreas LB, Smith AA, Ni QZ, Griffin RG. 2014. Paramagnet induced signal quenching in MAS-DNP experiments in frozen homogeneous solutions. *J. Magn. Reson.* 240:113–23
141. Akbey Ü, Franks WT, Linden A, Lange S, Griffin RG, et al. 2010. Dynamic nuclear polarization of deuterated proteins. *Angew. Chem. Int. Ed.* 49:7803–6
142. Mak-Jurkauskas ML, Bajaj VS, Hornstein MK, Belenky M, Temkin RJ, et al. 2008. Energy transformations early in the bacteriorhodopsin photocycle revealed by DNP-enhanced solid state NMR. *PNAS* 105:883–88
143. Bajaj V, Mak-Jurkauskas M, Belenky M, Herzfeld J, Griffin R. 2009. Functional and shunt states of bacteriorhodopsin resolved by 250 GHz dynamic nuclear polarization–enhanced solid-state NMR. *PNAS* 106:9244
144. Debelouchina GT, Bayro MJ, Fitzpatrick AW, Ladizhansky V, Colvin MT, et al. 2013. Higher order amyloid fibril structure by MAS NMR and DNP spectroscopy. *J. Am. Chem. Soc.* 135:19237–47
145. Lopez del Amo JM, Schneider D, Loquet A, Lange A, Reif B. 2013. Cryogenic solid state NMR studies of fibrils of the Alzheimer's disease amyloid-β peptide: perspectives for DNP. *J. Biomol. NMR* 56:359–63

146. Takahashi H, Ayala I, Bardet M, De Paëpe G, Simorre JP, Hediger S. 2013. Solid-state NMR on bacterial cells: selective cell wall signal enhancement and resolution improvement using dynamic nuclear polarization. *J. Am. Chem. Soc.* 135:5105–10
147. Salnikov E, Rosay M, Pawsey S, Ouari O, Tordo P, Bechinger B. 2010. Solid-state NMR spectroscopy of oriented membrane polypeptides at 100 K with signal enhancement by dynamic nuclear polarization. *J. Am. Chem. Soc.* 132:5940–41
148. Wang T, Park YB, Caporini MA, Rosay M, Zhong L, et al. 2013. Sensitivity-enhanced solid-state NMR detection of expansin's target in plant cell walls. *PNAS* 110:16444–49
149. Jacso T, Franks WT, Rose H, Fink U, Broecker J, et al. 2012. Characterization of membrane proteins in isolated native cellular membranes by dynamic nuclear polarization solid-state NMR spectroscopy without purification and reconstitution. *Angew. Chem. Int. Ed.* 51:432–35
150. Renault M, García J, Cordeiro TN, Baldus M, Pons M. 2013. Protein oligomers studied by solid-state NMR—the case of the full-length nucleoid-associated protein histone–like nucleoid structuring protein. *FEBS J.* 280:2916–28
151. Gelis I, Vitzthum V, Dhimole N, Caporini MA, Schedlbauer A, et al. 2013. Solid-state NMR enhanced by dynamic nuclear polarization as a novel tool for ribosome structural biology. *J. Biomol. NMR* 56:85–93
152. Reggie L, Lopez JJ, Collinson I, Glaubitz C, Lorch M. 2011. Dynamic nuclear polarization–enhanced solid-state NMR of a ^{13}C-labeled signal peptide bound to lipid-reconstituted Sec translocon. *J. Am. Chem. Soc.* 133:19084–86
153. Linden AH, Lange S, Franks WT, Akbey Ü, Specker E, et al. 2011. Neurotoxin II bound to acetylcholine receptors in native membranes studied by dynamic nuclear polarization NMR. *J. Am. Chem. Soc.* 133:19266–69
154. Ravera E, Corzilius B, Michaelis VK, Rosa C, Griffin RG, et al. 2013. Dynamic nuclear polarization of sedimented solutes. *J. Am. Chem. Soc.* 135:1641–44
155. Fricke P, Demers JP, Becker S, Lange A. 2014. Studies on the MxiH protein in T3SS needles using DNP-enhanced ssNMR spectroscopy. *ChemPhysChem* 15:57–60
156. Debelouchina GT, Bayro M, van der Wel PC, Caporini M, Barnes A, et al. 2010. Dynamic nuclear polarization–enhanced solid-state NMR spectroscopy of GNNQQNY nanocrystals and amyloid fibrils. *Phys. Chem. Chem. Phys.* 12:5911–19
157. Rosay M, Lansing JC, Haddad KC, Bachovchin WW, Herzfeld J, et al. 2003. High frequency dynamic nuclear polarization in MAS spectra of membrane and soluble proteins. *J. Am. Chem. Soc.* 125:13626–27
158. Sawaya MR, Sambashivan S, Nelson R, Ivanova MI, Sievers SA, et al. 2007. Atomic structures of amyloid cross-β spines reveal varied steric zippers. *Nature* 447:453–57
159. Loquet A, Giller K, Becker S, Lange A. 2010. Supramolecular interactions probed by ^{13}C–^{13}C solid-state NMR spectroscopy. *J. Am. Chem. Soc.* 132:15164–66
160. Caporini MA, Bajaj VS, Veshtort M, Fitzpatrick A, MacPhee CE, et al. 2010. High resolution determination of interstrand distances and alignment in amyloid fibrils. *J. Phys. Chem. B* 114:13555–61
161. Bateman DA, Tycko R, Wickner RB. 2011. Experimentally derived structural constraints for amyloid fibrils of wild-type transthyretin. *Biophys. J.* 101:2485–92
162. Lopez del Amo JM, Schneider D, Loquet A, Lange A, Reif B. 2013. Cryogenic solid state NMR studies of fibrils of the Alzheimer's disease amyloid-β peptide: perspectives for DNP. *J. Biomol. NMR* 56:359–63
163. Bajaj VS, van der Wel PC, Griffin RG. 2009. Observation of a low-temperature, dynamically driven structural transition in a polypeptide by solid-state NMR spectroscopy. *J. Am. Chem. Soc.* 131:118–28
164. Rossini AJ, Zagdoun A, Hegner F, Schwarzwälder M, Gajan D, et al. 2012. Dynamic nuclear polarization NMR spectroscopy of microcrystalline solids. *J. Am. Chem. Soc.* 134:16899–908
165. Takahashi H, Lee D, Dubois L, Bardet M, Hediger S, De Paëpe G. 2012. Rapid natural-abundance 2D ^{13}C–^{13}C correlation spectroscopy using dynamic nuclear polarization enhanced solid-state NMR and matrix-free sample preparation. *Angew. Chem. Int. Ed.* 51:11766–69
166. Takahashi H, Viverge B, Lee D, Rannou P, De Paëpe G. 2013. Towards structure determination of self-assembled peptides using dynamic nuclear polarization enhanced solid-state NMR spectroscopy. *Angew. Chem. Int. Ed.* 52:6979–82

167. Asami S, Szekely K, Schanda P, Meier BH, Reif B. 2012. Optimal degree of protonation for ^{1}H detection of aliphatic sites in randomly deuterated proteins as a function of the MAS frequency. *J. Biomol. NMR* 54:155–68
168. Linser R, Dasari M, Hiller M, Higman V, Fink U, et al. 2011. Proton-detected solid-state NMR spectroscopy of fibrillar and membrane proteins. *Angew. Chem. Int. Ed.* 50:4508–12
169. Asami S, Reif B. 2013. Proton-detected solid-state NMR spectroscopy at aliphatic sites: application to crystalline systems. *Acc. Chem. Res.* 46:2089–97
170. Chevelkov V, Rehbein K, Diehl A, Reif B. 2006. Ultrahigh resolution in proton solid-state NMR spectroscopy at high levels of deuteration. *Angew. Chem. Int. Ed.* 45:3878–81
171. Knight MJ, Felli IC, Pierattelli R, Bertini I, Emsley L, et al. 2012. Rapid measurement of pseudocontact shifts in metalloproteins by proton-detected solid-state NMR spectroscopy. *J. Am. Chem. Soc.* 134:14730–33
172. Lewandowski JR, Dumez J-N, Akbey Ü, Lange S, Emsley L, Oschkinat H. 2011. Enhanced resolution and coherence lifetimes in the solid-state NMR spectroscopy of perdeuterated proteins under ultrafast magic angle spinning. *J. Phys. Chem. Lett.* 2:2205–11
173. Linser R, Chevelkov V, Diehl A, Reif B. 2007. Sensitivity enhancement using paramagnetic relaxation in MAS solid-state NMR of perdeuterated proteins. *J. Magn. Reson.* 189:209–16
174. Zhou DH, Nieuwkoop AJ, Berthold DA, Comellas G, Sperling LJ, et al. 2012. Solid-state NMR analysis of membrane proteins and protein aggregates by proton detected spectroscopy. *J. Biomol. NMR* 54:291–305
175. Zheng L, Fishbein WK, Griffin RG, Herzfeld J. 1993. Two-dimensional solid-state proton NMR and proton exchange. *J. Am. Chem. Soc.* 6254–61
176. Zhou D, Shah G, Cormos M, Mullen C, Sandoz D, Rienstra C. 2007. Proton-detected solid-state NMR spectroscopy of fully protonated proteins at 40 kHz magic-angle spinning. *J. Am. Chem. Soc.* 129:11791–801
177. Paulson EK, Morcombe CR, Gaponenko V, Dancheck B, Byrd RA, Zilm KW. 2003. Sensitive high resolution inverse detection NMR spectroscopy of proteins in the solid state. *J. Am. Chem. Soc.* 125:15831–36
178. Ward ME, Shi L, Lake E, Krishnamurthy S, Hutchins H, et al. 2011. Proton-detected solid-state NMR reveals intramembrane polar networks in a seven-helical transmembrane protein proteorhodopsin. *J. Am. Chem. Soc.* 133:17434–43